

# Deep learning of committor and explainable artificial intelligence analysis for identifying reaction coordinates

Toshifumi Mori,<sup>1,2,3, a)</sup> Kei-ichi Okazaki,<sup>4,5, b)</sup> Kang Kim,<sup>6, c)</sup> and Nobuyuki Matubayasi<sup>6, d)</sup>

<sup>1)</sup>Department of Molecular Engineering, Graduate School of Engineering, Kyoto University, Kyoto 615-8510, Japan

<sup>2)</sup>Institute for Materials Chemistry and Engineering, Kyushu University, Kasuga, Fukuoka 816-8580, Japan

<sup>3)</sup>Interdisciplinary Graduate School of Engineering Sciences, Kyushu University, Kasuga, Fukuoka 816-8580, Japan

<sup>4)</sup>Research Center for Computational Science, Institute for Molecular Science, Okazaki, Aichi 444-8585, Japan

<sup>5)</sup>Graduate Institute for Advanced Studies, SOKENDAI, Okazaki, Aichi 444-8585, Japan

<sup>6)</sup>Division of Chemical Engineering, Department of Materials Engineering Science, Graduate School of Engineering Science, The University of Osaka, Toyonaka, Osaka 560-8531, Japan

(Dated: 27 March 2026)

In complex molecular systems, the reaction coordinate (RC) that characterizes transition pathways is essential to understand underlying molecular mechanisms. This review surveys a framework for identifying the RC by applying deep learning to the committor, which provides the most reliable measure of the progress along a transition path. The inputs to the neural network are collective variables (CVs) expressed as functions of atomic coordinates of the system, and the corresponding RC is predicted as the output by training the network on the committor as the learning target. Because deep learning models typically operate in a black-box manner, it is difficult to determine which input variables govern the predictions. The incorporation of eXplainable Artificial Intelligence (XAI) techniques enables quantitative assessment of the contributions of individual input variables to the predictions. This approach allows the identification of CVs that play dominant roles and demonstrates that the committor distribution on the surface using important CVs is separated by well-defined boundaries. The framework provides an explainable deep learning strategy for assigning a molecular mechanism from the RC and is applicable to a wide range of complex molecular systems.

## TABLE OF CONTENTS

<b>I. Introduction</b>	1
<b>II. Methods</b>	3
A. Committor as a measure for RC optimality	3
B. Cross entropy minimization	3
C. Neural network model for predicting RC	4
D. Input features as candidate CVs	4
E. XAI analysis	5
<b>III. Applications</b>	6
A. Alanine depeptide	6
B. Hyperparameter tuning	9
C. Ion dissociation	10
<b>IV. Summary and outlook</b>	13

## I. INTRODUCTION

Understanding the mechanisms of transition processes in complex molecular systems, as exemplified by protein con-

formational changes, nucleation, and solvation effects, is essential for characterizing the transition pathways that connect multiple stable states. However, the high dimensionality of these systems renders direct visualization and interpretation inherently difficult. One widely used approach to address this challenge is the potential of mean force (PMF).<sup>1</sup>

The PMF is referred to as the free-energy landscape, and more specifically is defined as the free energy as a function of a collective variable (CV)  $x$ , which is *a priori* selected from the atomic coordinate space  $\mathbf{R} = (\mathbf{r}_1, \mathbf{r}_2, \dots, \mathbf{r}_N)$  describing the positions of  $N$  atoms:

$$F(x) = -k_B T \ln \int e^{-U(\mathbf{R})/k_B T} \delta[x - x(\mathbf{R})] d\mathbf{R}, \quad (1)$$

where  $k_B$ ,  $T$ , and  $U(\mathbf{R})$  denote the Boltzmann constant, temperature, and potential energy of the system. Typical CVs are commonly defined in terms of interatomic distances, bond angles, and dihedral angles that characterize molecular conformation changes. For example, the radial distribution function  $g(r)$  with respect to the interatomic distance  $r$  can be interpreted as a PMF. Calculating the PMF in molecular dynamics (MD) simulations of complex molecular systems is a central challenge, and various sampling methods, including umbrella sampling,<sup>2</sup> the replica exchange method,<sup>3</sup> and metadynamics,<sup>4</sup> have been developed to address the high computational cost associated with exhaustive configurational sampling.<sup>5-8</sup>

The term “collective variable” is often used interchangeably with “order parameter”, but the latter typically refer to a CV that distinguishes between reactant and product states. Furthermore, “reaction coordinate” can be regarded as an order

<sup>a)</sup>Electronic mail: toshi\_mori@moleng.kyoto-u.ac.jp

<sup>b)</sup>Electronic mail: keokazaki@ims.ac.jp

<sup>c)</sup>Electronic mail: kk@cheng.es.osaka-u.ac.jp

<sup>d)</sup>Electronic mail: nobuyuki@cheng.es.osaka-u.ac.jp

parameter that characterizes the dynamical progress from reactant to product states.<sup>9</sup> Specifically, within the framework of transition state theory, when a saddle point on the PMF corresponds to the transition state (TS), the selected CV serves as the reaction coordinate (RC).<sup>9</sup> In this case, transitions from reactant to product states necessarily proceed via barrier crossing along the RC. However, identifying an appropriate CV that is truly relevant to the RC among many candidate CVs is inherently nontrivial. A critical issue is that the free-energy barrier on the PMF may depend on the selection of CVs.<sup>1,10,11</sup> This highlights the necessity of rigorously examining whether a given PMF can correctly capture the TS.

The committor analysis is a statistical approach for identifying the RC from transition paths sampled in MD simulations.<sup>12–17</sup> Here, states A and B denote reactant and product states, respectively, separated by the TS. The committor  $p_B^*(\mathbf{R})$  is defined as the probability of trajectories, initiated from an arbitrary configuration  $\mathbf{R}$  with velocities randomly drawn from the Maxwell–Boltzmann distribution, that reaches state B prior to A. If the initial configuration  $\mathbf{R}$  locates at the TS, the probabilities of reaching A and B are equal, yielding  $p_B^* = 1/2$ . In other words, the TS can be characterized as the set of configurations exhibiting  $p_B^* = 1/2$ . In practice, the committor analysis requires evaluating the distribution  $p(p_B^*)$  from an ensemble of configurations sampled in the vicinity of the saddle point and assessing whether the selected CV is appropriate based on the presence of a sharp peak at  $p_B^* = 1/2$ . This committor distribution test has been widely applied to assess the quality of selected CVs across a variety of complex molecular systems.<sup>18–46</sup>

The committor analysis is a reliable method; however, its trial-and-error nature, which depends strongly on physical intuition, limits its efficiency and motivates the development of more systematic approaches.<sup>47–50</sup> Machine learning approaches based on committor analysis for identifying RCs have attracted considerable attention and have led to the development of various methodological frameworks. Ma and Dinner introduced a genetic neural network method and applied it to committor values evaluated for molecular configurations.<sup>51</sup> Peters *et al.* developed a method based on maximum likelihood estimation to identify the RC.<sup>52,53</sup> By combining aimless shooting, a variant of transition path sampling, with a procedure that maximizes the log-likelihood, they introduced a framework for quantifying the contributions of candidate CVs to the RC. The aimless shooting yields a binary outcome for each trajectory initiated from a given initial configuration, generating instantaneous committor values (or observed commitments)  $p_B^* = 0$  or 1, corresponding to states A and B, respectively. The committor is modeled using a sigmoidal function,  $p_B(q) = [1 + \tanh(q)]/2$ , and maximization of the long-likelihood based on these binary outcomes determines the optimal RC. Here,  $q$  is ultimately expressed as a linear combination of the candidate CVs associated with the initial configurations. This likelihood-based optimization approach has been widely applied for identifying RCs in a broad range of studies.<sup>54–80</sup> Other machine learning methodologies for identifying RCs that characterize transition pathways have also been developed.<sup>81–119</sup> Moreover, numerous review arti-

cles have appeared in recent years.<sup>120–128</sup>

Recently, we developed a deep learning framework trained on committor values  $p_B^*$  of configurations sampled near the saddle point region from MD simulations.<sup>129</sup> The schematic illustration of the work flow is shown in Fig. 1. In this approach, candidate CVs are employed as input features to a neural network, and the corresponding RC is predicted as the output by training the network using  $p_B^*$  as the learning target. The cross-entropy, which quantifies the discrepancy between the sigmoidal function,  $p_B(q) = [1 + \tanh(q)]/2$ , and the pre-evaluated committor values  $p_B^*$  that vary continuously from 0 to 1, is employed as a loss function and is minimized during training.<sup>130,131</sup> This formulation extends the likelihood maximization in that the cross-entropy is derived from the Kullback–Leibler (KL) divergence by expressing the likelihood in logarithmic form.<sup>130</sup>

Because deep learning models often behave as black-boxes, eXplainable AI (XAI) techniques are further employed to quantify the contribution of each input variable to predictions.<sup>133,134</sup> XAI can be regarded as a class of model-agnostic interpretation methods for deep learning models. As major implementations of XAI, we employed Local Interpretable Model-agnostic Explanations (LIME)<sup>135</sup> and the game theory-based framework known as Shapley Additive exPlanations (SHAP)<sup>136</sup>. XAI approach enables the identification of CVs with significant contribution, providing a representation of the TS on the free-energy landscape that is consistent with the underlying transition pathways. As an application, we investigated the isomerization reaction of alanine dipeptide and identified specific dihedral angles as the primary contributor to the RC.<sup>129</sup> We also demonstrated that the isomerization can also be characterized by specific interatomic distances.<sup>137</sup> Moreover, we investigated how hyperparameters in the neural network model influences the performance and reliability of the identified RC.<sup>132</sup> Furthermore, we investigated the RC for NaCl ion dissociation–association process in water. In particular, to describe the solvent environment surrounding the ions, we employed atom-centered symmetry functions (ACSFs), which are widely used as descriptors in machine learning potentials,<sup>138–140</sup> as input CVs to the neural network.<sup>141</sup>

Other studies have provided interpretability for RCs identified through committor based deep learning approaches. Frassek *et al.* reported the application of an autoencoder architecture comprising an encoder, a reconstruction decoder, and a committor decoder to obtain low-dimensional representations of RCs from a large set of input CVs.<sup>142</sup> Jung *et al.* introduced a sampling method that determines relevant RCs using maximum likelihood estimation combined with deep learning, and further employed symbolic regression to derive interpretable mathematical expressions representing trained models.<sup>143</sup> Neumann and Schwierz applied a related deep learning framework to predict the RC governing magnesium binding to RNA and used permutation importance to quantify feature relevance from the input CVs.<sup>144</sup> Naleem *et al.* investigated RCs for the committor using 17 machine learning models, including Light Gradient Boosting Machine (LGBM) based on the decision tree method<sup>145</sup>, and quantified input CVs contributions with SHAP.<sup>146</sup> Their results showed

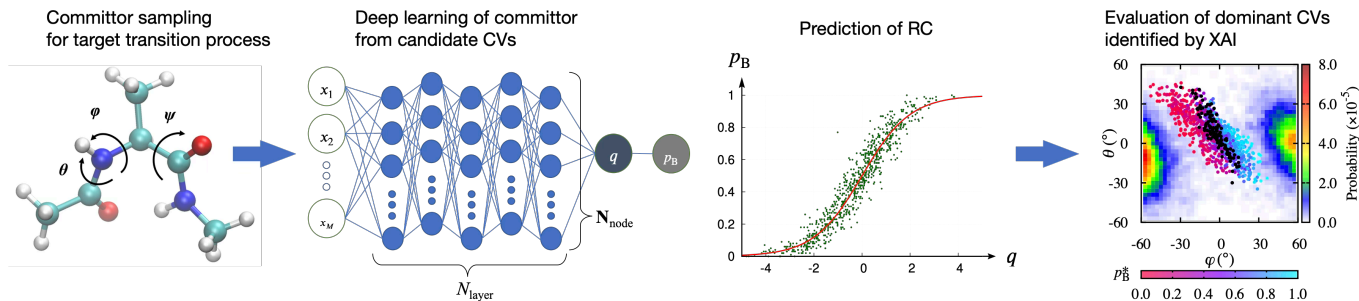


FIG. 1. Schematic illustration of the explainable deep learning framework for identifying RCs based on committor  $p_B^*$  sampling. First, MD trajectories are generated to sample the committor  $p_B^*$  for the target transition process. The candidate CVs,  $x_i$ , are utilized as input features and mapped to the output  $q$  by a neural network model of  $N_{\text{layer}}$  consisting of  $N_{\text{node}}$ . The neural network is trained such that the committor  $p_B^*$  follows a sigmoidal function  $p_B(q) = [1 + \tanh(q)]/2$ , where  $q$  serves as the RC. Finally, XAI analysis identifies the dominant CVs contributing to the RC  $q$ , enabling evaluation of the committor  $p_B^*$  distribution on the corresponding free-energy landscape. Reproduced from Y. Mori, K.-i. Okazaki, T. Mori, K. Kim, and N. Matubayasi, J. Chem. Phys. **153**, 054115 (2020),<sup>131</sup> with the permission of AIP Publishing, K. Kawashima, T. Sato, K.-i. Okazaki, K. Kim, N. Matubayasi, and T. Mori, APL Mach. Learn **3**, 016113 (2025)<sup>132</sup>; licensed under a Creative Commons Attribution (CC BY) license, and T. Kikutsuji, Y. Mori, K.-i. Okazaki, T. Mori, K. Kim, and N. Matubayasi, J. Chem. Phys. **156**, 154108 (2022)<sup>129</sup>; licensed under a Creative Commons Attribution (CC BY) license.

that the combination of LGBM and SHAP yielded the most robust description of alanine dipeptide isomerization.

This review introduces an explainable deep learning framework based on the committor for identifying the RC and its applications to complex molecular systems. The structure of this review is as follows. Section II outlines the background and methodology of our explainable deep learning approach. Section III presents the applications to isomerization of alanine dipeptide and ion-pair dissociation in water, and discusses the hyperparameter tuning of the neural network. Section IV provides a summary and an outlook.

## II. METHODS

### A. Committor as a measure for RC optimality

Committor  $p_B^*(\mathbf{R})$  is defined as a probability to reach state B prior to reaching state A from a given coordinate  $\mathbf{R}$  in a two-state system with states A and B. A naive approach to calculate  $p_B^*$  is to perform multiple short MD simulations with velocities randomly generated from a Maxwell–Boltzmann distribution and count the probability of reaching state B.  $p_B^*$  is 0 when  $\mathbf{R}$  is near state A whereas it becomes 1 near state B. At the TS,  $p_B^*$  is expected to be 0.5, *i.e.*, there is equal chance of reaching states A and B. In high dimensional systems, it is often convenient to describe the system with a RC  $q$  that connects states A and B and construct a PMF along  $q$ . Ideally, the committor as a function of  $q$ ,  $p_B(q)$ , is expected to smoothly change monotonically from 0 (at state A), pass 0.5 (at TS), and reach 1 (at state B). Thus, committor can be used as a measure to evaluate the quality of the reaction coordinate  $q$ . The monotonic change of the committor as a function of a reaction coordinate has been modeled using several functions including the sigmoidal function  $[1 + \tanh(q)]/2$  and error function  $\text{erfc}(-q)/2$ .<sup>9,130</sup> While the sigmoidal function is more popular due to the relevance with the neural network framework, the

error function also has an advantage for its relationship with the Kramers–Langer–Berezhevskii–Szabo theory.<sup>27,49,131</sup>

In practice, obtaining a RC that shows an ideal curve of  $p_B(q)$  is often highly challenging. Thus, committor can serve as a measure to examine the quality of a given RC. From a set of points  $\{k\}$  with  $q^{(k)} = f(\mathbf{R}^{(k)})$  and  $p_B^*(k) = p_B^*(\mathbf{R}^{(k)})$ , the adequacy of a trial RC  $q$  can be examined by comparing  $p_B^*(k)$  from the ideal curve  $p_B(q)$ .

### B. Cross entropy minimization

The discrepancy between the modeled and pre-evaluated committors along a trial reaction coordinate, denoted as  $p_B(q^{(k)})$  and  $p_B^*(k)$ , respectively, can be assessed by comparing the  $p_B$  and  $p_B^*$  distributions using the KL divergence  $\mathcal{D}_{\text{KL}}$ ,

$$\begin{aligned} \mathcal{D}_{\text{KL}}(p_B^* \| p_B) &= \sum_k \sum_{I=A,B} p_I^*(k) \ln \frac{p_I^*(k)}{p_I(q^{(k)})} \\ &= \sum_k \left\{ p_B^*(k) \ln \frac{p_B^*(k)}{p_B(q^{(k)})} \right. \\ &\quad \left. + (1 - p_B^*(k)) \ln \frac{1 - p_B^*(k)}{1 - p_B(q^{(k)})} \right\}, \quad (2) \end{aligned}$$

where  $q^{(k)}$  is a trial RC at point  $k$ ,  $p_B(q^{(k)})$  is the model function that describe the change of  $p_B$  along  $q$ , and  $p_A^*(k)$  and  $p_A(q^{(k)})$  satisfy  $p_A^*(k) = 1 - p_B^*(k)$  and  $p_A(q^{(k)}) = 1 - p_B(q^{(k)})$ , respectively.  $\mathcal{D}_{\text{KL}}(p_B^* \| p_B)$  is a measure to quantify the difference in the distribution of  $p_B^*$  from  $p_B$ .  $\mathcal{D}_{\text{KL}}$  satisfies  $\mathcal{D}_{\text{KL}}(p_B^* \| p_B) \geq 0$  and becomes 0 only when the two distributions match exactly. Thus,  $\mathcal{D}_{\text{KL}} = 0$  for an ideal RC, and finding an ideal RC is equivalent to minimizing Eq. (2).

$\mathcal{D}_{\text{KL}}$  can be divided into the self- and cross-entropy terms

( $\mathcal{H}_S$  and  $\mathcal{H}_X$ , respectively)

$$\mathcal{D}_{\text{KL}}(p_{\text{B}}^* \| p_{\text{B}}) = -\mathcal{H}_S(p_{\text{B}}^*) + \mathcal{H}_X(p_{\text{B}}^*, p_{\text{B}}), \quad (3)$$

where

$$\begin{aligned} \mathcal{H}_S(p_{\text{B}}^*) &= -\sum_k p_{\text{B}}^*(k) \ln p_{\text{B}}^*(k) \\ &\quad - \sum_k [1 - p_{\text{B}}^*(k)] \ln [1 - p_{\text{B}}^*(k)] \end{aligned} \quad (4)$$

and

$$\begin{aligned} \mathcal{H}_X(p_{\text{B}}^*, p_{\text{B}}) &= -\sum_k p_{\text{B}}^* \ln p_{\text{B}}(q^{(k)}) \\ &\quad - \sum_k [1 - p_{\text{B}}^*] \ln [1 - p_{\text{B}}(q^{(k)})]. \end{aligned} \quad (5)$$

As the self-entropy term is invariant to changes in the trial reaction coordinate  $q$ , minimizing  $\mathcal{D}_{\text{KL}}$  is equivalent to minimizing the cross-entropy term. The following objective function  $\mathcal{L}$  is thus defined to quantify the difference between the modeled and pre-evaluated committors:

$$\mathcal{L}(q) = \mathcal{H}_X(p_{\text{B}}^*, p_{\text{B}}(q)) + \lambda G(q). \quad (6)$$

Note that the first term is a generalization of the log-likelihood maximization.<sup>52,53</sup> The second term describes the penalty function applied to  $q$  so as to suppress overfitting and  $\lambda$  is the regularization parameter that controls the penalty term. An example is the  $L_2$  norm regularization.<sup>131</sup> By minimizing Eq. (6), a RC  $q$  that most closely mimic the monotonic behavior, *e.g.*,  $p_{\text{B}}(q) = [1 + \tanh(q)]/2$ , can be obtained.

### C. Neural network model for predicting RC

The RC  $q$  is obtained as a function of the coordinate  $\mathbf{R}$ . However, the mapping from  $\mathbf{R}$  to  $q$  is nontrivial. In many cases, the system  $\mathbf{R}$  is first described with pre-selected set of CVs. The RC is defined as a function of the CVs, either in a linear or nonlinear form. Deep neural network (DNN) model is a nonlinear mapping approach to obtain the RC from the candidate CVs. In DNN, the candidate CVs, discussed in Section II D, serves as the input features ( $\mathbf{x}$ ) after standardization, and  $q$  is obtained as the output. A common model is the multilayer perceptron model, which consists of  $N_{\text{layers}}$  hidden layers and  $N_{\text{node}}$  nodes (Fig. 1). Further choices of the model includes the activation function (the leaky rectified linear unit (Leaky ReLU) or scaled ExponentialLinear Unit), and regularizations ( $L_1$ ,  $L_2$ , etc). These parameters, *i.e.* hyperparameters, needs to be chosen prior to optimizing the DNN model, and choosing the hyperparameters are unfortunately nontrivial and highly tedious. Here we only consider leaky ReLU with a leaky parameter set of 0.01, and utilize  $L_2$  regularization. The number of hidden layers were also fixed to five with 400, 200, 400, 200, and 400 nodes, and the dropout at a rate of 0.5 was set to every layer in Secs. III A and III C. The effect of hyperparameters to the model result are discussed in Section III B.

### D. Input features as candidate CVs

The construction of CVs used as input features is a crucial aspect of committor based machine learning for identifying RCs. In the study by Ma and Dinner on the isomerization of alanine dipeptide, pairwise distances, bond angles, and dihedral angles, including improper dihedrals, were employed as inputs to a genetic neural network.<sup>51</sup> Furthermore, to investigate the RC for isomerization in explicit solvents, it is necessary to incorporate CVs that explicitly describe solute-solvent and solvent-solvent interactions. In particular, CVs such as the solvent accessible surface area, radius of gyration, and excluded volume of the solute, as well as density fields defined on spherical polar coordinate grids and energetic, force, and torque components within the solute molecule, have been considered.<sup>51</sup> Section III A outlines our deep learning study of the isomerization reaction of alanine dipeptide. We considered 45 dihedral angles, including improper ones. To account for the periodicity of dihedral angles, both cosine and sine forms were used, generating a total of 90 CVs. Section III B further describes our study of neural network hyperparameter tuning using the alanine dipeptide in water system. In that work, the electrostatic and van der Waals potentials from solvents to solute atoms were included in addition to dihedral angles, resulting in a total of 134 CVs.

Another complex molecular system in which solvent effects play a central role is gas hydrate nucleation, for which a variety of CVs have been examined. The nucleus size is commonly quantified using the mutually coordinated guest parameter, which counts the number of gas molecules participating in the largest solid nucleus in the system.<sup>147</sup> In addition, the number of water molecules incorporated into the nucleus and the cage types of the growing nucleus are also employed as CVs.<sup>73</sup> Other CVs include the bond-orientational order parameters proposed by Steinhardt<sup>148</sup>, and their variants<sup>149</sup> were used in similar liquid-solid nucleation systems.<sup>60</sup>

Furthermore, the CV construction becomes challenging in solvent-mediated ion pair dissociation. Müllen *et al.* applied the inertial likelihood maximization method,<sup>61</sup> an extension of the likelihood maximization that incorporating the velocity, acceleration, and jerk of the inter-ion distance  $r_{\text{ion}}$ , to NaCl ion pair dissociation in water.<sup>65</sup> In this approach, a total of 71 candidate CVs representing water bridging structures, namely, configurations in which the O and H atoms of a water molecule simultaneously coordinate to the Na and Cl ions, respectively, were considered. It was demonstrated that the inter-ionic water density  $\rho$  and the number of bridging waters  $N_{\text{B}}$  contribute most significantly to the RC. Specifically, the inter-ionic water density  $\rho$  is defined as

$$\rho = \left( \frac{1}{2\pi\sigma^2} \right)^{3/2} \sum_w \exp\left( -\frac{|\mathbf{r}_w - \mathbf{r}_{\text{mid}}|^2}{2\sigma^2} \right), \quad (7)$$

where  $\mathbf{r}_w$  denotes the center-of-mass position of the  $w$ -th water molecule and  $\mathbf{r}_{\text{mid}}$  is the midpoint between the Na and Cl ions. The parameter  $\sigma$  controls the effective volume over which water molecules are counted and is chosen as  $r_{\text{ion}}/2$ . The number of bridging waters  $N_{\text{B}}$  is evaluated in two steps. First, the

ion–water coordination function is defined as

$$f_{s-w} = \frac{1 - \tanh[a(R_{s-w} - b)]}{2}, \quad (8)$$

where the subscript  $s$  denotes the ion species (Na or Cl). The distance  $R_{s-w}$  corresponds to the distance between the Na ion and the  $w$ -th water O atom for Na coordination, and between the Cl ion and the  $w$ -th water H atom for Cl coordination. The parameters are set to  $a = 3 \text{ \AA}^{-1}$  and  $b = 3.2 \text{ \AA}$ . The number of water molecules simultaneously coordinating both ions is then given by

$$N_B = \sum_w \min(f_{\text{Na}-w}, f_{\text{Cl}-w}). \quad (9)$$

In particular,  $\rho$  and  $N_B$  were identified as important CVs, together with the ion–ion distance  $r_{\text{ion}}$ , through analyses of the PMF.<sup>65,70,150–156</sup> These studies showed that the formation of water bridges lowers the dissociation free energy barrier and facilitates ion pair dissociation.

Jung *et al.* recently employed atom-centered symmetry functions (ACSFs) as CVs to represent the solvent environment in studies of ion pair dissociation.<sup>143</sup> ACSFs are commonly used as descriptors in machine learning potentials,<sup>138–140</sup> and quantify the distribution of neighboring atoms at specific distances and angles around a reference atom.<sup>139</sup> Because they are invariant under translational and rotational operations, ACSFs provide a systematic representation of local solvent environment. To represent the solvent environment around the ions, two types of ACSFs,  $G_i^2$  and  $G_i^5$  for reference atom  $i$ , were employed as input variables for neural networks.<sup>143</sup> Here, these ACSFs are defined as

$$G_i^{2,Z_1} = \sum_{j \neq i}^{|Z_1|} e^{-\eta(R_{ij}-R_s)^2} \cdot f_c(R_{ij}), \quad (10)$$

$$G_i^{5,Z_1,Z_2} = 2^{1-\zeta} \sum_{j \neq i}^{|Z_1|} \sum_{k \neq i}^{|Z_2|} (1 + \lambda \cos \theta_{ijk})^\zeta \cdot e^{-\eta((R_{ij}-R_s)^2 + (R_{ik}-R_s)^2)} \cdot f_c(R_{ij}) \cdot f_c(R_{ik}), \quad (11)$$

respectively. Note that  $R_{ij}$  ( $R_{ik}$ ) represents the distance between atoms  $i$  and  $j$  ( $k$ ), and  $\theta_{ijk}$  denotes the angle formed by atoms  $j$  and  $k$  with atom  $i$  at the center.  $Z_1$  and  $Z_2$  represent atomic species surrounding the reference atom and the absolute value notation denotes their respective atomic numbers. Furthermore, the cut-off function is introduced as

$$f_c(R_{ij}) = \begin{cases} 0.5 \cdot [\cos(\pi R_{ij}/R_c) + 1] & \text{for } R_{ij} < R_c \\ 0 & \text{for } R_{ij} > R_c, \end{cases} \quad (12)$$

with the cut-off radius,  $R_c$ .

The ACSF  $G_i^2$  is defined as the sum of a Gaussian function weighted by the cutoff function. The width of the Gaussian is determined by the parameter  $\eta$ , while its center can be positioned at a specific radial distance using the parameter  $R_s$ . This function is particularly suitable for characterizing the spherical shell environment surrounding a reference atom.

The ACSF  $G_i^5$  extends  $G_i^2$  by incorporating an additional target atom and including an angular component. The parameter  $\lambda$  can take values of 1 or  $-1$ , shifting the maximum of the cosine function to  $\theta_{ijk} = 0^\circ$  and  $\theta_{ijk} = 180^\circ$ , respectively. The parameter  $\zeta$  controls the angular resolution, with larger values of  $\zeta$  corresponding to a narrower range of nonzero contributions in the ACSF. Section III C outlines our explainable deep learning framework for ion pair dissociation, in which a total of 1,296 ACSFs are used as CVs. The correlations between water bridging structures described by  $\rho$  and  $N_B$  and the ACSFs identified by the SHAP analysis are further discussed.

## E. XAI analysis

XAI was applied to interpret committor predictions obtained from neural network training. Because deep-learning models are highly complex, direct identification of interpretable features is difficult. To address this issue, we employed XAI techniques, LIME and SHAP, to quantify the contribution of each input variable to the predictions of the black-box classifier through model-agnostic interpretable models.

LIME enables interpretation of the contribution of individual input variables in a black-box neural network through an interpretable surrogate model.<sup>135</sup> Specifically, LIME constructs a local explanation model based on linear regression that approximates the behavior of the original model in the vicinity of the data point of interest. In this context, input variables associated with large regression coefficients provide insight into the prediction. The interpretable feature  $\xi(\mathbf{x})$  is obtained by fitting a linear regression model  $g$  to the predictions of the black-box model  $f$ , represented by the neural network, for the input data  $\mathbf{x}$ . This procedure is formulated as

$$\xi(\mathbf{x}) = \operatorname{argmin}_{g \in G} (L(f, g, \pi_x) + \Omega(g)), \quad (13)$$

where  $L(f, g, \pi_x)$  denotes a loss function that quantifies the discrepancy between the predictions of  $f$  and  $g$ , and  $G$  represents the class of candidate explanation models. The regularization term  $\Omega(g)$  penalizes model complexity to promote interpretability. Specifically,  $L(f, g, \pi_x^{\text{LIME}})$  is defined as

$$L(f, g, \pi_x^{\text{LIME}}) = \sum_{\mathbf{z}, \mathbf{z}' \in Z} \pi_x^{\text{LIME}}(\mathbf{z})(f(\mathbf{z}) - g(\mathbf{z}'))^2, \quad (14)$$

where  $\pi_x^{\text{LIME}}$  denotes the proximity measure characterizing the locality around the input data  $\mathbf{x}$  to be explained.

In practice, perturbed samples  $\mathbf{z}$  generated around  $\mathbf{x}$  and weighted by the proximity measure are mapped onto binary variables  $\mathbf{z}' \in \{0, 1\}^M$ , where  $M$  denotes the number of input variables, to provide a human-interpretable representation, because the components of the original input space are not always directly interpretable. The proximity measure is further given by

$$\pi_x^{\text{LIME}}(\mathbf{z}) = \exp(-D(\mathbf{x}, \mathbf{z})^2/\sigma^2), \quad (15)$$

where  $D$  is a distance metric and  $\sigma$  controls the width of the neighborhood. By minimizing the object function, LIME

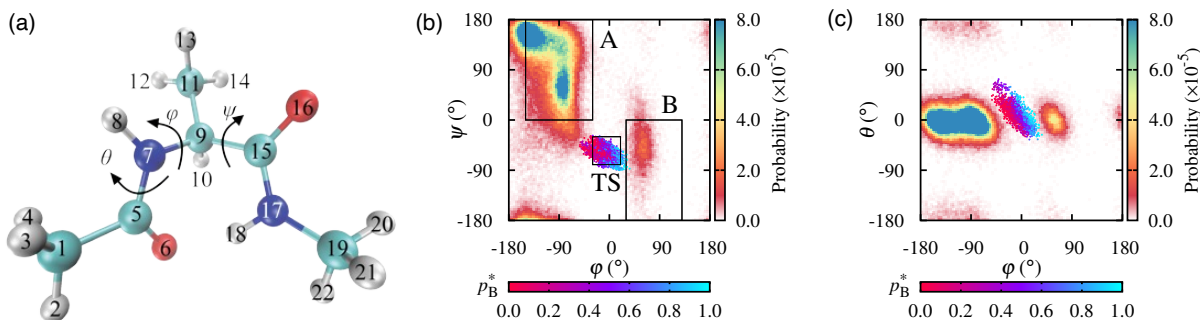


FIG. 2. (a) Atomic indices assigned to alanine dipeptide. The three major dihedral angles,  $\varphi$ ,  $\psi$ , and  $\theta$ , are indicated. (b) Probability distribution in the  $(\varphi, \psi)$  plane. The dashed lines define state A  $[(-150^\circ, 0^\circ) \leq (\varphi, \psi) \leq (30^\circ, 180^\circ)]$ , state B  $[(30^\circ, -180^\circ) \leq (\varphi, \psi) \leq (130^\circ, 0^\circ)]$ , and the intermediate region TS  $[(-30^\circ, -80^\circ) \leq (\varphi, \psi) \leq (20^\circ, -30^\circ)]$ . (c) Probability distribution in the  $(\varphi, \theta)$  plane. In (b) and (c), points are colored according to the committer value  $p_B^*$ , as indicated by the color bar. Reproduced from T. Kikutsuji, Y. Mori, K.-i. Okazaki, T. Mori, K. Kim, and N. Matubayasi, *J. Chem. Phys.* **156**, 154108 (2022)<sup>129</sup>; licensed under a Creative Commons Attribution (CC BY) license.

yields a local surrogate model  $g$  that approximates the behavior of  $f$  near  $\mathbf{x}$ , from which the interpretable feature  $\xi(\mathbf{x})$  is obtained.

Furthermore, SHAP, a game-theory-based method, was applied. Whereas LIME assumes that local model behavior can be approximated by linear regression, SHAP enforces an additive decomposition in which the sum of individual feature contributions equals the predicted value.<sup>136</sup> In SHAP, an additive feature attribution method provides a linear function consisting of binary variables:

$$g(\mathbf{z}') = \phi_0 + \sum_{i=1}^M \phi_i z'_i. \quad (16)$$

Here,  $\phi_0$  denotes the bias term, and  $\phi_i$  represents the contribution of the  $i$ -th feature  $x'_i$ , which is an interpretable representation corresponding to the original input variable  $x_i$ . SHAP determines the coefficients  $\phi_i$  using Shapley values, which originate from game theory and allocate contributions among features.<sup>157</sup> Note that LIME can be understood as an additive feature attribution method that provides linear models in the binary vector space in the sense that the explanation model  $g$  of LIME can be expressed by Eq. (16). Exact computation of Shapley values requires evaluation over all permutations of feature inclusion, which is generally computationally demanding. To address this limitation, Kernel SHAP was introduced to approximate the Shapley values efficiently. In Kernel SHAP, the coefficients  $\phi_i$  are obtained by solving a weighted linear regression problem, thereby quantifying the contribution of each feature to the model prediction.

Specifically, for Kernel SHAP, the following equations are used with Eq. (13) of the LIME algorithm:

$$\Omega(g) = 0, \quad (17)$$

$$\pi_x^{\text{SHAP}}(\mathbf{z}') = \frac{M-1}{M C_{|\mathbf{z}'|} |\mathbf{z}'| (M - |\mathbf{z}'|)}, \quad (18)$$

$$L(f, g, \pi_x^{\text{SHAP}}) = \sum_{\mathbf{z}' \in \mathcal{Z}} \pi_x^{\text{SHAP}}(\mathbf{z}') (f(h_x^{-1}(\mathbf{z}')) - g(\mathbf{z}'))^2, \quad (19)$$

where  $|\mathbf{z}'|$  is the number of non-zero features in  $\mathbf{z}'$  and  $h_x$  is

a mapping function of binary variables  $\mathbf{z}'$  into the original input data  $\mathbf{x}$ . The local explanation model  $g(\mathbf{z}')$  approximating  $f(h_x^{-1}(\mathbf{z}'))$  can be obtained using a weighted linear regression with Eq. (18), which differs from the weight function used in LIME, as shown in Eq. (15). Note the contrast between Eqs. (15) and (18), which are used in LIME and SHAP, respectively. In practice, if we use SHAP's kernel of Eq. (18) as LIME's kernel, LIME will provide values similar to SHAP values.

The choice between LIME and SHAP, or the consistent use of both, merits consideration. SHAP, developed as an additive feature attribution method and closely related to LIME, and the features identified as having large contributions by LIME and by SHAP are therefore expected to be consistent. Because LIME generates perturbed samples randomly, the resulting explanations may vary between runs. This variability can be reduced by increasing the number of generated perturbed samples. SHAP offers a theoretical foundation grounded in game theory. By decomposing the predicted value into contributions that are fairly allocated among features, SHAP provides a more sophisticated quantification of individual contributions than LIME. However, the computational cost of SHAP increases exponentially with the number of features since the evaluation of Shapley values requires consideration of many feature combinations.

### III. APPLICATIONS

#### A. Alanine dipeptide

Bolhuis *et al.* applied the committer analysis to the isomerization reaction of alanine dipeptide<sup>20</sup>. The Ramachandran plot, which represents the probability distribution of the backbone dihedral angles  $\varphi$  and  $\psi$ , is commonly used to characterize protein conformation (see Figure 2(a) for the definitions of  $\varphi$  and  $\psi$ ).<sup>158</sup> This plot can be regarded as the PMF defined in terms of two CVs,  $\varphi$  and  $\psi$ . In vacuum, two energetically stable conformations are observed: the  $\beta$ -sheet structure (state A)

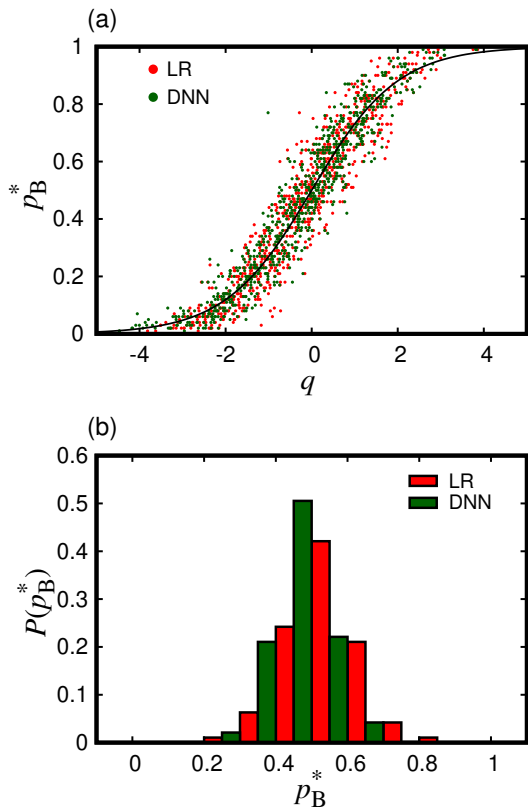


FIG. 3. (a) Relationship between the committor value  $p_B^*$  and the RC  $q$  predicted by LR (red) and DNN (green) for the test dataset (800 points). The black solid line denotes the sigmoidal function  $p_B(q) = [1 + \tanh(q)]/2$ . (b) Probability distribution of the committor  $p_B^*$  obtained from LR (red) and DNN (green) within the range  $-0.2 < q < 0.2$  shown in (a). Reproduced from T. Kikutsuji, Y. Mori, K.-i. Okazaki, T. Mori, K. Kim, and N. Matubayasi, *J. Chem. Phys.* **156**, 154108 (2022)<sup>129</sup>; licensed under a Creative Commons Attribution (CC BY) license.

and the left-handed  $\alpha$ -helix structure (state B) (see Figure 2(b) for the definitions of states A and B). However, analysis of the committor distribution obtained by sampling initial configurations  $x$  in the vicinity of the saddle point showed that the distribution does not exhibit a peak at  $p_B^* = 1/2$ , but instead is nearly uniform over the interval from 0 to 1. This behavior indicates that the saddle point on the PMF does not necessarily correspond to the TS. They further demonstrated that inclusion of an additional dihedral angle  $\theta$  is required for the committor distribution to develop a peak at  $p_B^* = 1/2$  (see Figure 2(a) for the definition of  $\theta$ ). Thus, although the Ramachandran plot based on  $\varphi$  and  $\psi$  distinguishes states A and B, incorporation of  $\theta$  is necessary to represent the RC appropriately.

We applied the explainable deep learning framework to the isomerization reaction of alanine dipeptide in vacuum. State A was defined by  $(-150^\circ, 0^\circ) \leq (\varphi, \psi) \leq (30^\circ, 180^\circ)$ , whereas state B was defined by  $(30^\circ, -180^\circ) \leq (\varphi, \psi) \leq (130^\circ, 0^\circ)$ .

An intermediate region corresponding to the expected TS,  $(-30^\circ, -80^\circ) \leq (\varphi, \psi) \leq (20^\circ, -30^\circ)$ , was also defined, from which 2,000 initial configurations were sampled using the aimless shooting. For each configuration, velocities were assigned randomly according to the Maxwell–Boltzmann distribution at 300 K, and 100 trajectories of 1 ps duration were generated to evaluate the committor value  $p_B^*$ . For each initial configuration, a total of 90 collective variables ( $M = 90$ ) were constructed by including both cosine and sine representations of all 45 dihedral angles in the molecule (see Table I of Ref. 129 for the correspondence between CV indices and dihedral angles). Figures 2(b) and 2(c) show the distributions of the sampled configurations, colored by the committor value  $p_B^*$ . Figure 2(c) displays the distribution obtained when  $\varphi$  and  $\theta$  were chosen as the collective variables. While configurations with  $p_B^* \approx 1/2$  are broadly dispersed on the  $(\varphi, \psi)$  plane, a more distinct separatrix line emerges on the  $(\varphi, \theta)$  plane. This observation indicates that  $\theta$ , rather than  $\psi$ , contributes more directly to the RC, in agreement with previous findings reported by Bolhuis *et al.*<sup>20</sup>

A dataset comprising dihedral angles and committor values from 2,000 initial configurations was divided into training, validation, and test sets in a 5:1:4 ratio. For comparison, linear regression (LR) implemented through a single-layer perceptron was also carried out, where  $q$  is expressed as  $q = w_0 + \sum_{m=1}^M w_m x_m$  with coefficients  $(w_0, w_1, \dots, w_M)$ , including the bias term  $w_0$ . All other calculation conditions are described in the original paper.<sup>129</sup>

The learned models of LR and DNN predict the relationship between the committor value  $p_B^*$  and the reaction coordinate  $q$  from the test dataset (800 samples). Figure 3(a) shows the committor value  $p_B^*$  as a function of  $q$  for the test dataset. In both cases,  $p_B^*$  follows a sigmoidal dependence, indicating successful learning. To further examine the behavior near  $q = 0$ , the probability distribution of  $p_B^*$  in the range of  $-0.2 < q < 0.2$  is presented in Figure 3(b). For both LR and DNN,  $p_B^*$  exhibits a clear peak at  $1/2$ . These results demonstrate that the RC  $q$  predicted by the LR and DNN models appropriately characterizes the isomerization reaction of alanine dipeptide. The configurations near  $q = 0$ , corresponding to  $p_B \approx 1/2$ , can be therefore regarded as the TS.

We quantified the contributions of grouped input variables to the reaction coordinate  $q$  predicted by the DNN using LIME and SHAP. Specifically, the dataset of 2,000 configurations was first partitioned into three regions:  $0 \leq p_B^* < 0.1$  (near state A),  $0.49 < p_B^* < 0.51$  (near the TS), and  $0.9 < p_B^* \leq 1$  (near state B). Within each region, 30 configurations were randomly selected and analyzed using LIME and SHAP to quantify the contribution of each input variable to the predicted RC. Figure 4 presents the absolute values of the average feature contributions obtained from LIME and SHAP across the three regions. For comparison, the absolute values of the coefficients  $(w_1, w_2, \dots, w_{90})$  derived from the LR model are also shown in Figure 4. The feature contributions identified by LIME and SHAP exhibit trends that closely match the coefficients obtained from linear regression. Table II of Ref. 129 lists the five dihedral angles with the largest absolute contribution values.

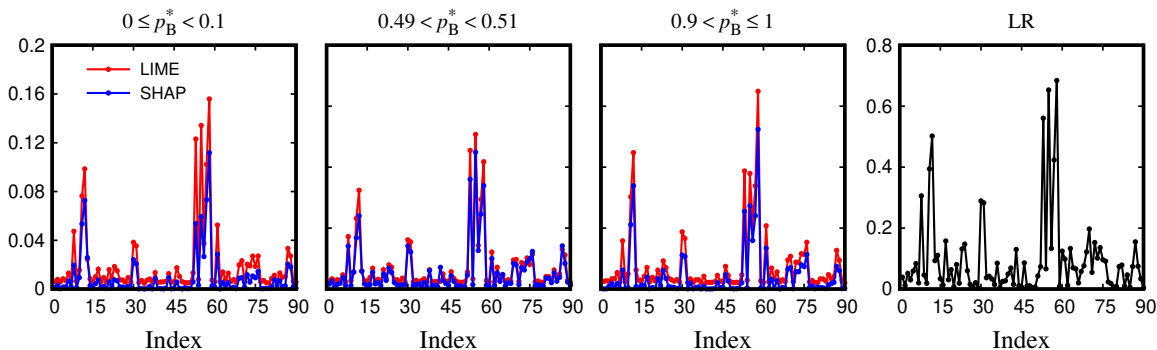


FIG. 4. Feature contribution of each CV in absolute value obtained using LIME (red) and SHAP (blue). From left to right:  $0 \leq p_B^* < 0.1$  (near state A),  $0.49 < p_B^* < 0.51$  (near TS), and  $0.9 < p_B^* \leq 1$  (near state B). The rightmost panel shows the absolute values of the coefficients ( $w_1, w_2, \dots, w_{90}$ ) obtained from the LR model. Reproduced from T. Kikutsuji, Y. Mori, K.-i. Okazaki, T. Mori, K. Kim, and N. Matubayasi, *J. Chem. Phys.* **156**, 154108 (2022)<sup>129</sup>; licensed under a Creative Commons Attribution (CC BY) license.

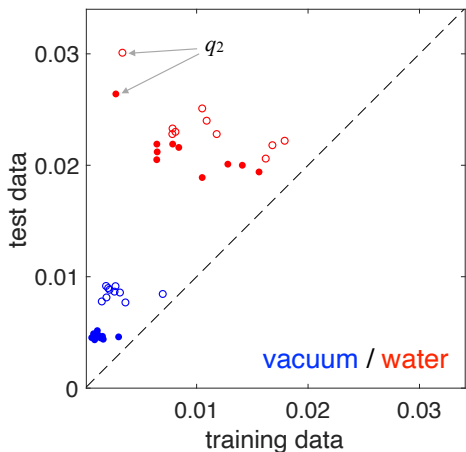


FIG. 5. Scatter plot for RMSEs between the predicted and reference  $p_B$  for the training and test data sets. Filled and open circles indicate the RMSEs using full points and those at about the TS ( $-0.2 < q_i < 0.2$ ), respectively. Blue and red colors are the results in vacuum and water.  $q_2$  in water shows a sign of slight overfitting, yet the RMSE against the test data is only marginally larger than the other RCs. Reproduced from K. Kawashima, T. Sato, K.-i. Okazaki, K. Kim, N. Matubayasi, and T. Mori, *APL Mach. Learn* **3**, 016113 (2025)<sup>132</sup>; licensed under a Creative Commons Attribution (CC BY) license.

Indices 57 and 54, which rank highest in the LR model, correspond to  $\sin \varphi$  (5–7–9–11) and  $\sin \theta$  (6–7–8–9), respectively. This result indicates that the dihedral angle governing changes in  $\varphi$  is  $\theta$  rather than  $\psi$ . As discussed above, comparison of Figures 2(b) and 2(c) shows that configurations with  $p_B^* \approx 1/2$  form a more distinct separatrix line on the  $(\varphi, \theta)$  plane than on the  $(\varphi, \psi)$  plane, consistent with this explanation. Both LIME and SHAP further indicate that the dihedral angles  $\varphi$  (Indices 11, 56, and 57) and  $\theta$  (Indices 52 and 54) make substantial contributions to the DNN-based prediction model. The results obtained from LIME and SHAP are largely consistent across the three  $p_B^*$  regions, indicating agreement between LIME and SHAP in the present analysis. Remark-

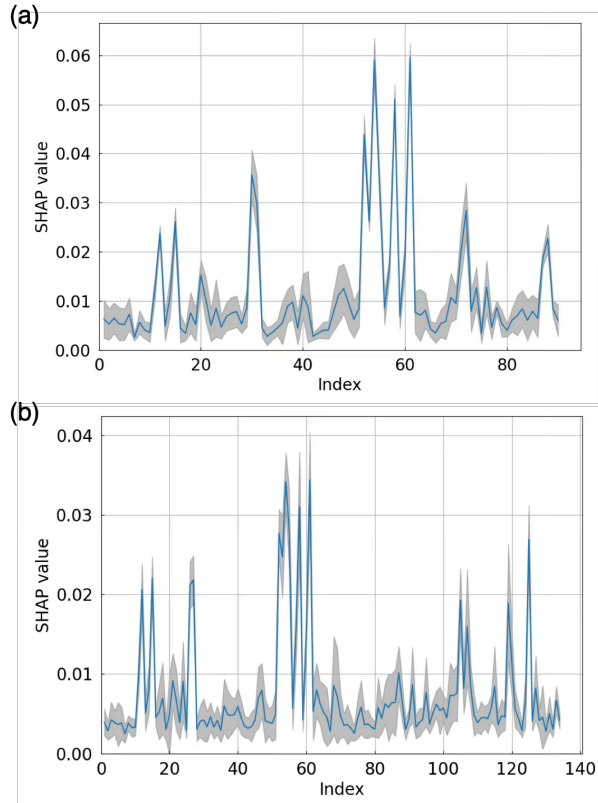


FIG. 6. Feature contributions of each CV in absolute value using SHAP for cases in (a) vacuum and (b) water. Blue lines and gray shades denote the average and variance calculated from the ten optimized RCs. Reproduced from K. Kawashima, T. Sato, K.-i. Okazaki, K. Kim, N. Matubayasi, and T. Mori, *APL Mach. Learn* **3**, 016113 (2025)<sup>132</sup>; licensed under a Creative Commons Attribution (CC BY) license.

ably, both LIME and SHAP reveal that the most dominant contribution shifts from  $\varphi$  to  $\theta$  for configurations near the TS region ( $0.49 < p_B^* < 0.51$ ), in contrast to configurations close

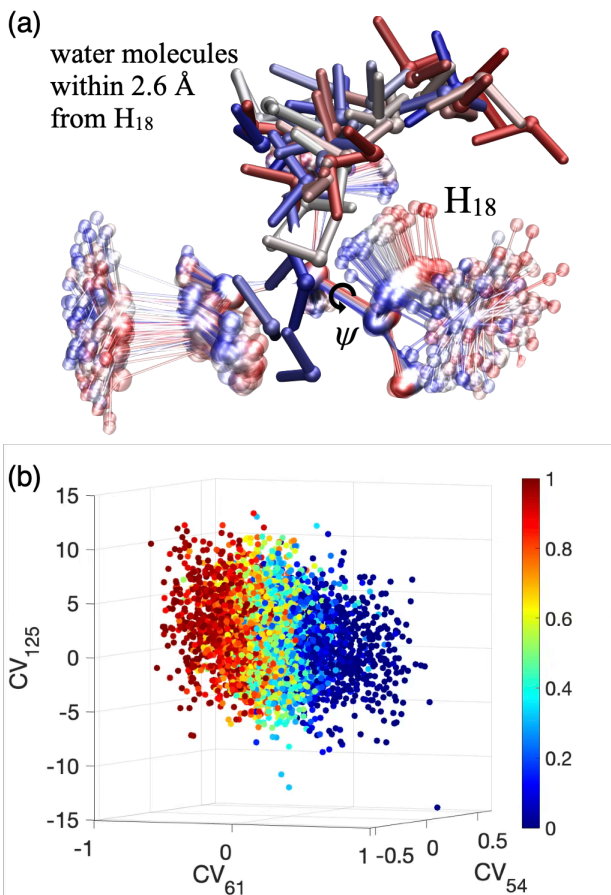


FIG. 7. (a) Structures within  $|q_1| < 0.2$  sorted based on  $\psi$  and aligned against the backbone atoms of alanine. RWB color range indicate the change of  $\psi$  in the structures from  $-123^\circ$  to  $-50^\circ$ . Water molecules within  $2.6 \text{ \AA}$  from  $H_{18}$  is shown. Alanine dipeptide and water molecules are shown in blurry and sharp representations, respectively. (b) Correlations between the changes in CVs and  $p_B$  in water. Reproduced from K. Kawashima, T. Sato, K.-i. Okazaki, K. Kim, N. Matubayasi, and T. Mori, *APL Mach. Learn* **3**, 016113 (2025)<sup>132</sup>; licensed under a Creative Commons Attribution (CC BY) license.

to state A ( $0 \leq p_B^* < 0.1$ ) or state B ( $0.9 < p_B^* \leq 1$ ). This distinction can be interpreted as follows: near the TS, variations in  $\theta$  induce a stronger influence than variations in  $\varphi$ , which accounts for the larger contribution to the conformation change. Indeed, as shown in Figure 2(c), the separatrix line defined by  $p_B^* = 1/2$  is tilted with respect to the  $\varphi$  axis. This geometry indicates that variations in  $\theta$  are essential for barrier crossing. Such specific TS features cannot be captured by the global coefficients ( $w_1, w_2, \dots, w_{90}$ ) of the LR model. Instead, they are revealed through local explanation models applied to DNN predictions using XAI techniques such as LIME and SHAP.

## B. Hyperparameter tuning

As demonstrated in Sec. III A, DNN model can describe the RC quite effectively. On the other hand, the hyperparameters,

e.g. the number of hidden layers, nodes per hidden layer, and regularization penalty, need to be defined prior to optimizing the DNN model. Choosing the hyperparameters can affect the performance of the DNN model and is a highly tedious task, the adequacy of the chosen hyperparameters remain ambiguous. Neumann and Schwierz<sup>144</sup> have applied the Keras Tuner random search hyperparameter optimization to automatically determine the DNN model for the magnesium binding to RNA. Nevertheless, how the choice of hyperparameters affects the quality and outcome of the DNN model remains unexplored. Finding the appropriate set of hyperparameters thus remains highly tedious and nontrivial task.

The hyperparameter tuning framework using the Bayesian optimization method with a Gaussian process was applied to the isomerization reaction of alanine dipeptide in vacuum and in water. The hyperparameter space of the DNN model for RCs in the two cases were optimized and explored. The number of hidden layers ( $N_{\text{layer}}$ ), node per hidden layer ( $N_{\text{node}}$ ), and  $L_2$  regularization parameter for each hidden layer  $\lambda$  were chosen as the hyperparameters and determined automatically. The isomerization reactions of alanine dipeptide in vacuum and in water solution were studied. The data points with committor values and CVs were collected using the transition path sampling method. The CV consists of 45 dihedral angles in cosine and sine forms following the previous section for the reaction in vacuum. The electrostatic and van der Waals (vdW) interactions from the waters to the atoms in alanine dipeptide were additionally adopted in the reaction in water. The number of CVs were thus 90 and 134 for cases in vacuum and water, respectively. The details of the system setup and sampling procedures are described in Ref. 132. 3714 and 4590 points were generated for the reactions in vacuum and in water, respectively. States A and B were simply defined as  $\phi \leq -30$  and  $\phi \geq 30$ .

The hyperparameters were searched from 2 to 5 for  $N_{\text{layer}}$ , from 100 to 5000 with 100 increments for  $N_{\text{node}}$ , and from 0.0001 to 0.1000 with 20 points equally spaced in a logarithmic scale for  $\lambda$ , respectively. Note that  $N_{\text{node}}$  and  $\lambda$  were chosen separately for each hidden layer. The initial values for these parameters were chosen randomly within the exploration range, and 10 models were constructed using different initial seeds for each system to see where the hyperparameters converge. Bayesian optimization was performed for 150 trials, and DNN model was trained for a maximum of 1000 epochs using the cross-entropy function as the loss function for each hyperparameter set. Early stopping was applied when the value of the loss function did not improve for five consecutive steps. The data was divided into training and validation sets at a ratio of 8:2 and training, validation, and into training, validation, and test sets at a ratio of 5:1:4 during hyperparameter training and final DNN training, respectively.

The optimized hyperparameters for the reactions in vacuum and water are summarized in Table I and II of Ref. 132. In both cases, the hyperparameters from different initial seeds ended up in different optimal parameter sets, thus did not converge to a unique minimum.  $N_{\text{node}}$  most frequently converged to 5 and 3 in vacuum and in water, respectively. The number of nodes  $N_{\text{node}}$  ranged from 100 to 5000 and differed between

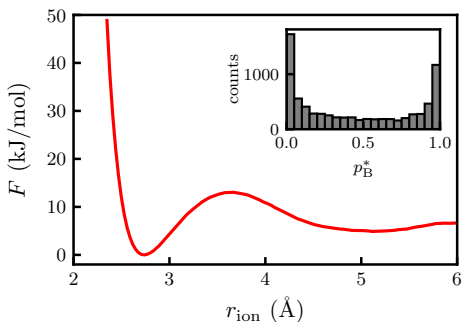


FIG. 8. PMF  $F(r_{\text{ion}})$  as a function of the interionic distance  $r_{\text{ion}}$ . The point with the minimum energy is set to 0 kJ/mol. Inset: Distribution of Committor  $p_B^*$  evaluated for configurations sampled within the range  $3.2 \text{ \AA} < r_{\text{ion}} < 4.3 \text{ \AA}$ . Reproduced from Ke. Okada, Ka. Okada, K.-i. Okazaki, T. Mori, K. Kim, and N. Matubayasi, J. Chem. Phys. **164**, 094101 (2026),<sup>141</sup> with the permission of AIP Publishing.

the hidden layers. The regularization parameter  $\lambda$  also converged to various values, and were generally larger in water than in vacuum. The difference in  $\lambda$  implies that the larger number of CV candidates as input require larger penalty to suppress overfitting. The root-mean-square errors (RMSE) between the predicted ( $p_B$ ) and reference ( $p_B^*$ ) committor values, shown in Fig. 5, showed that RMSE in vacuum was smaller than those in water. On the other hand, while the RMSEs for the training data showed some variations especially in the case in water, those for the test data were comparable between the RCs, e.g., the means were about 0.004 and 0.02 in vacuum and in water, respectively. These results indicate that the RCs show similar performance despite the difference in the hyperparameters. We also note that the RCs were found to be highly similar, e.g., the correlation coefficients between the coordinates calculated using the data points were mostly  $> 0.99$  (see Figs. S4 and S9 of Ref. 132).

The CVs contributing to the optimized RCs were also analyzed using LIME and SHAP. Fig. 6 summarizes the feature contributions of CVs in vacuum and water obtained with SHAP. The features with notable contributions in vacuum were consistent with those obtained in Section III A. Moreover, the RCs showed very similar trends as seen by the small variances. In water, the electrostatic potential from water on  $H_{18}$ , the hydrogen attached to the backbone nitrogen of C-terminal N-methylamide (Fig. 2a), were found to have large contribution as well as the torsion angles  $\phi$  and  $\psi$ , represented by indices 54 and 61. Interestingly, this resembles the solvent-derived electrostatic torque for a different path ( $C_{7\text{eq}} \rightarrow \alpha_R$  transition)<sup>51</sup>. This suggests that the isomerization of a backbone of alanine dipeptide in water is induced by a water molecule interacting with the proton attached to the backbone, thereby triggering the twisting motion of the backbone. Indeed, Fig. 7a shows that, depending on the position of the closest water to  $H_{18}$ , the N-CA-C-N torsion angle is altered by the displacement of  $H_{18}$ . The correlation between CVs with indices 54, 61, and 125 and  $p_B$ , seen in the 3D scatter plot in Fig. 7b, also shows that CV<sub>125</sub> is correlated with  $p_B$

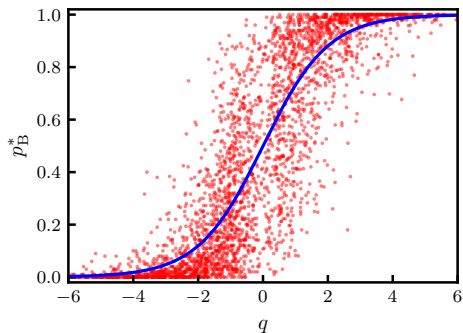


FIG. 9. Committor  $p_B^*$  as a function of the RC  $q$  predicted by DNN trained model using the test dataset (3,040 points). The blue curve represents the sigmoidal function,  $p_B(q) = [1 + \tanh(q)]/2$ . Reproduced from Ke. Okada, Ka. Okada, K.-i. Okazaki, T. Mori, K. Kim, and N. Matubayasi, J. Chem. Phys. **164**, 094101 (2026),<sup>141</sup> with the permission of AIP Publishing.

and thus contributes to the RC.

### C. Ion dissociation

The association and dissociation of ion pairs in water are fundamental processes in physical chemistry, yet their RCs are complex, involving not only the interionic distance but also solvent-mediated hydration structures. This process may appear to be adequately described by the interionic distance,  $r_{\text{ion}}$ .<sup>159–166</sup> However,  $r_{\text{ion}}$  alone does not fully capture the underlying mechanism. Previous studies for NaCl ion pairs in water have shown that the committor distribution of configurations sampled near the saddle point of the PMF defined  $r_{\text{ion}}$  is bimodal, with peaks near  $p_B^* \approx 0$  and 1.<sup>19,35</sup> This behavior indicates that configurations sharing the same interionic distance  $r_{\text{ion}}$  can follow distinct transition pathways toward either association or dissociation, highlighting the essential role of the surrounding water structure in determining the reaction. Specifically, at the TS, a bridging configuration is expected to form in which the O and H atoms of a water molecule simultaneously coordinate to the Na and Cl ions, respectively. Geissler *et al.* proposed a mechanism in which a water molecule initially coordinating the Na ion migrates toward the Cl-ion side, thereby creating space for additional water molecules to enter.<sup>19</sup> Consequently, changes in the coordination number of water molecules near the ions at the TS are thought to facilitate activation of the dissociation process.

We applied an explainable deep learning framework to identify the RC for the association and dissociation of a NaCl ion pair in TIP/4p-Ew water. Detailed MD calculations are described in our prior study.<sup>141</sup> The architecture of the DNN is the same as that used in Section III A. A total of 7,600 configurations were extracted via umbrella sampling within the interionic distance range,  $3.2 \text{ \AA} < r_{\text{ion}} < 4.3 \text{ \AA}$ . This range was chosen to cover the saddle point located at  $r_{\text{ion}} = 3.6 \text{ \AA}$  on the PMF defined by  $r_{\text{ion}}$ , as shown in Fig. 8. The associated state A is defined by  $r_{\text{ion}} < 3.2 \text{ \AA}$ , and the dissociated state B by  $r_{\text{ion}} > 4.3 \text{ \AA}$ . The committor value,  $p_B^*$  for each sampled

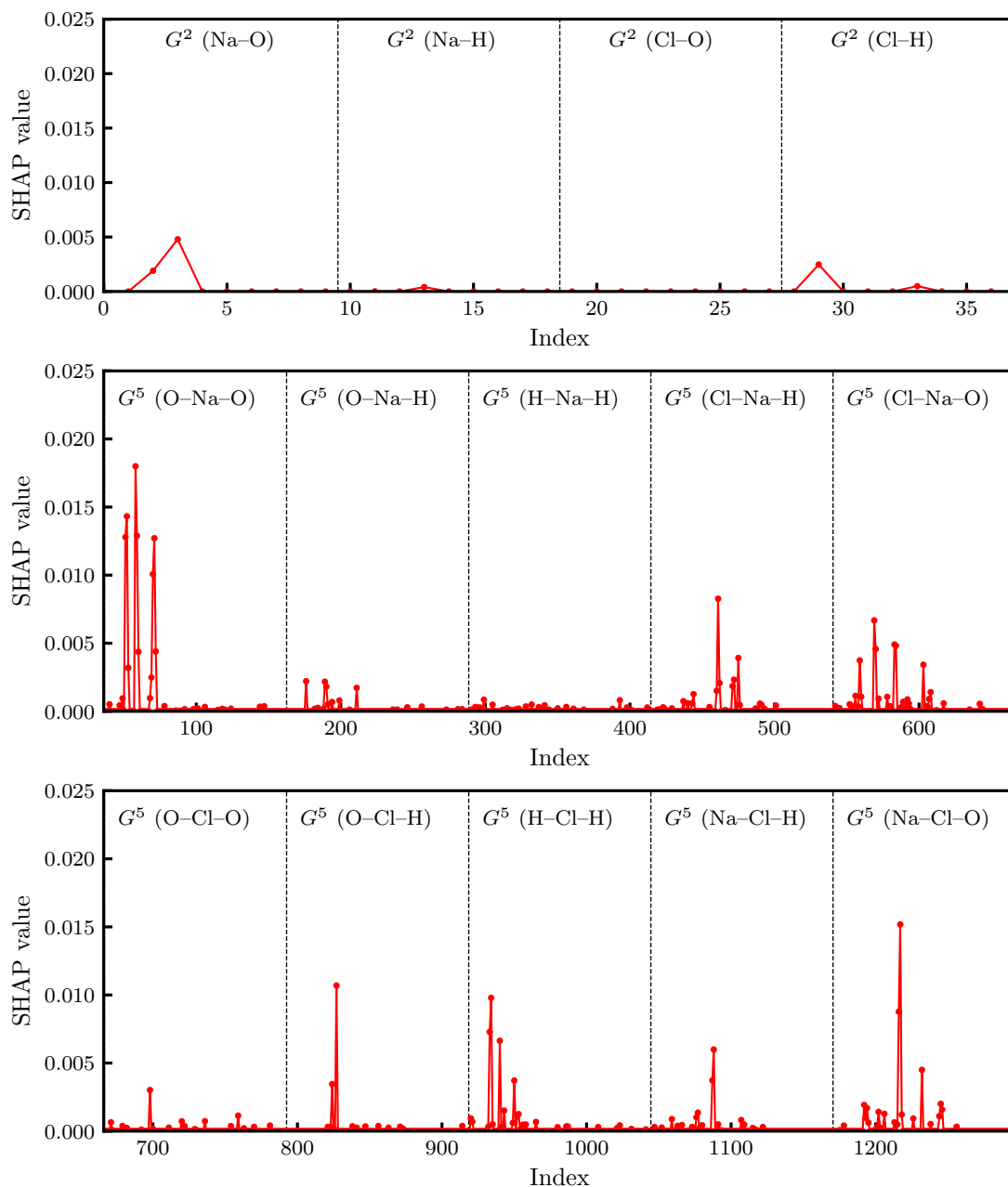


FIG. 10. Index dependence of feature contribution of each CV evaluated by the absolute SHAP value. Reproduced from Ke. Okada, Ka. Okada, K.-i. Okazaki, T. Mori, K. Kim, and N. Matubayasi, *J. Chem. Phys.* **164**, 094101 (2026),<sup>141</sup> with the permission of AIP Publishing.

configuration was evaluated by assigning initial velocities randomly drawn from the corresponding Maxwell–Boltzmann distribution of 300 K and performing 100 independent 1 ps MD simulations. The resulting distribution of  $p_B^*$  is shown in the inset of Fig. 8. The committer values are biased toward 0 and 1, with no pronounced peak near 0.5, consistent with observations reported in previous studies.<sup>19,35</sup> In this study, two types of ACSFs describing the solvent environment around the ions,  $G^2$  and  $G^5$ , were employed as CVs for the neural network inputs (see definitions of ACSFs in Section IID). For  $G^2$ , the cutoff radius was set to  $R_c = 10.0 \text{ \AA}$  with  $\eta = 2.0 \text{ \AA}^{-2}$ , while for  $G^5$ ,  $\eta = 1.2 \text{ \AA}^{-2}$  was used. For  $G^2$ , four atomic

combinations were considered:  $(i-Z_1) = (\text{Na-O}), (\text{Na-H}), (\text{Cl-O}),$  and  $(\text{Cl-H})$ . For  $G^5$ , the following 10 combinations were included:  $(Z_1 - i - Z_2) = (\text{O-Na-O}), (\text{O-Na-H}), (\text{H-Na-H}), (\text{Cl-Na-H}), (\text{Cl-Na-O}), (\text{O-Cl-O}), (\text{O-Cl-H}), (\text{H-Cl-H}), (\text{Na-Cl-H}),$  and  $(\text{Na-Cl-O})$ . By systematically varying the remaining parameters  $R_s$ ,  $\lambda$ , and  $\zeta$ , we generated a total of 1,296 CVs comprising 36  $G^2$  and 1,260  $G^5$  CVs. Detailed definitions of the  $G^2$  and  $G^5$  input features are provided in Table S1 of Ref. 141. The dataset was divided into training, validation, and test sets in a 5:1:4 ratio. All input variables were standardized prior to neural network training. Other computational details for DNN are described in our paper.<sup>141</sup>

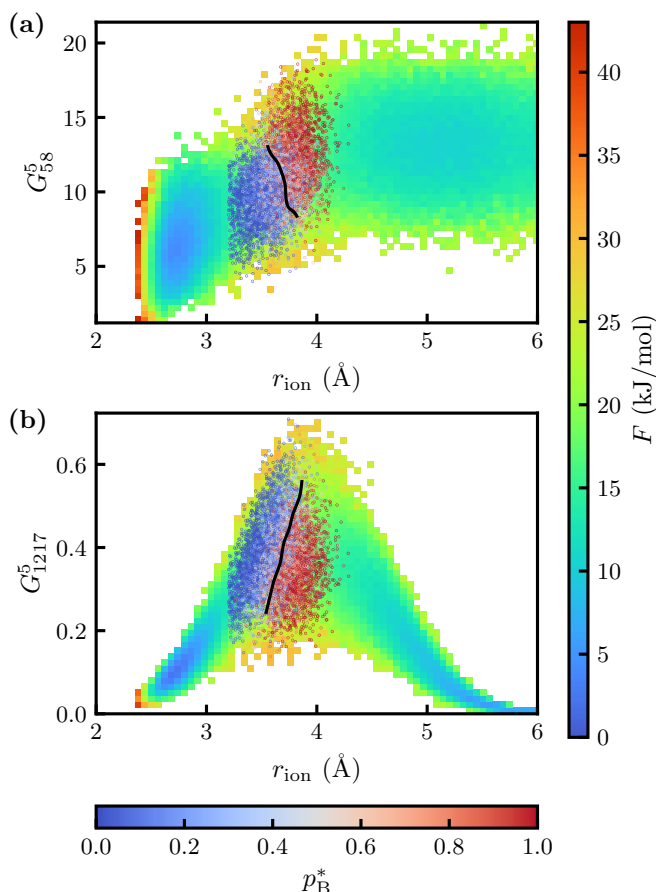


FIG. 11. Two-dimensional PMF using the interionic distance  $r_{\text{ion}}$  and  $G_{58}^5$  (a) and  $G_{1217}^5$  (b). The point with the minimum energy is set to 0 kJ/mol, and values are color-coded according to the color bar on the right. Committer values  $p_B^*$  are colored according to the bottom color bar. The black lines are drawn as follows. The ranges of the x- and y-axis values were each divided into 200 grid points (forming a  $200 \times 200$  grid), and the average committer value  $p_B^*$  within each grid cell was computed. After applying cubic interpolation for smoothing, contour lines corresponding to  $p_B^* = 0.5$  were plotted. Reproduced from Ke. Okada, Ka. Okada, K.-i. Okazaki, T. Mori, K. Kim, and N. Matubayasi, J. Chem. Phys. **164**, 094101 (2026),<sup>141</sup> with the permission of AIP Publishing.

Figure 9 presents the learning results of the DNN for the committer,  $p_B^*$ . It is shown that the relationship between  $p_B^*$  and  $q$  for the test dataset has sufficiently converged to the sigmoidal function,  $p_B(q) = [1 + \tanh(q)]/2$ . However, the committer values near  $q = 0$  are widely distributed between 0 and 1 and do not exhibit a clear sharp peak at  $p_B^* = 1/2$ . This behavior is likely due to the substantially larger number of input variables compared to the alanine dipeptide case (see Section III A). It is expected to be overcome in future study through approaches such as hyperparameter tuning, as discussed in Section III B. The contribution of each input variable to the RC  $q$  predicted by the DNN was evaluated using SHAP. The absolute SHAP value for each index was computed for 100 configurations randomly sampled from the test dataset, and their average is shown in Fig. 10. Tables I and

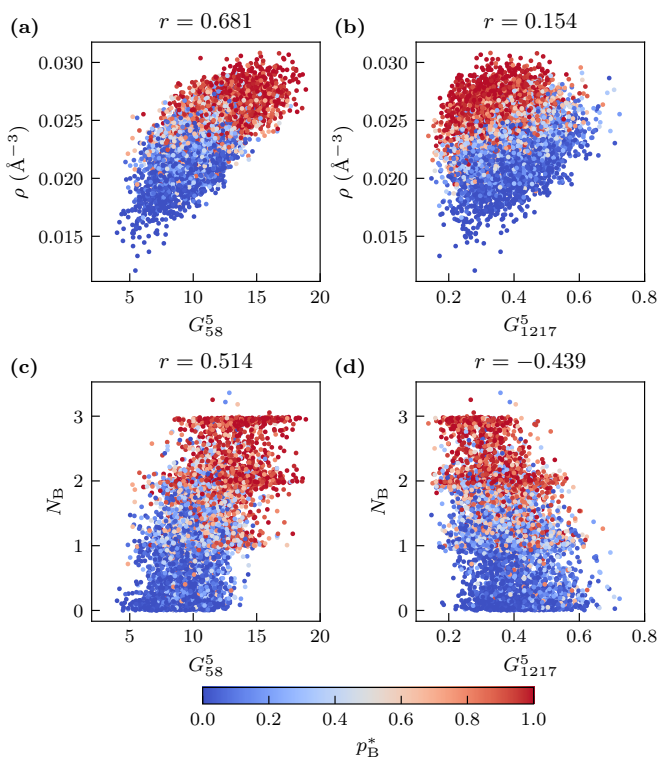


FIG. 12. Distribution of committer  $p_B^*$  dataset in the two-dimensional surface using the combinations  $(G_{58}^5, \rho)$  (a),  $(G_{1217}^5, \rho)$  (b),  $(G_{58}^5, N_B)$  (c), and  $(G_{1217}^5, N_B)$  (d). Committer values are colored according to the bottom color bar. The  $r$ -value represents the correlation coefficient for each panel. Reproduced from Ke. Okada, Ka. Okada, K.-i. Okazaki, T. Mori, K. Kim, and N. Matubayasi, J. Chem. Phys. **164**, 094101 (2026),<sup>141</sup> with the permission of AIP Publishing.

II of Ref. 141 show the top five contributing factors and their corresponding absolute SHAP values for (O-Na-O) and (Na-Cl-O) descriptors, respectively.

The  $G^5$  at index 58 (denoted as  $G_{58}^5$ ) shows the largest contribution and corresponds to the O-Na-O combination, with distance sensitivity  $R_s = 2.0 \text{ \AA}$ , angular sensitivity  $\lambda = -1$ , and  $\zeta = 1$ . This indicates that water O atoms located within a spherical shell of radius  $R_s = 2.0 \text{ \AA}$  centered on the Na ion make a dominant contribution. Notably,  $R_s = 2.0 \text{ \AA}$  is nearly equal to the Lennard-Jones diameter of Na ion. In contrast, the low angular resolution  $\zeta = 1$  implies that angular dependence plays a minor role in characterizing the distribution of O atoms around Na ion. The  $G^5$  at index 1217 (denoted as  $G_{1217}^5$ ) corresponding to the (Na-Cl-O) combination, exhibits a second highest contribution following the RC and is characterized by  $R_s = 4.0 \text{ \AA}$ ,  $\lambda = 1$ , and  $\zeta = 16$ . At this high angular sensitivity, the angular component  $2^{1-\zeta}(1 + \cos \theta_{ijk})^\zeta$  decreases from unity and approaches zero near  $\theta_{ijk} \approx 60^\circ$ . This indicates that the dominant Na-Cl-O bond angles lie within this range, suggesting that water O atoms located in the overlapping region of the hydration shells, namely, at a Na-Cl separation of  $R_s = 4.0 \text{ \AA}$  that is slightly larger than the PMF saddle point distance  $r_{\text{ion}} = 3.6 \text{ \AA}$ , are a primary contributing factor.

Based on these results, it is expected that  $G_{58}^5$  or  $G_{1217}^5$  will

appropriately represent the RC together with the interionic distance  $r_{\text{ion}}$ . Figure 11(a) and (b) show the two-dimensional PMFs constructed using  $(r_{\text{ion}}, G_{58}^5)$  and  $(r_{\text{ion}}, G_{1217}^5)$ , respectively. The distribution of committers  $p_B^*$  are also shown on the corresponding  $(r_{\text{ion}}, G_{58}^5)$  and  $(r_{\text{ion}}, G_{1217}^5)$  planes. In these figures, the committor  $p_B^*$  varies continuously from the associated state A ( $p_B^* \approx 0$ ) to the dissociated state B ( $p_B^* \approx 1$ ), with the TS ( $p_B^* = 0.5$ ) forming a well defined separatrix line. Figure 11(a) shows that, when the interionic distance  $r_{\text{ion}}$  is fixed at the saddle point of the PMF,  $r_{\text{ion}} = 3.6 \text{ \AA}$ , the committor increases with increasing  $G_{58}^5$ , indicating that the arrangement of water O atoms surrounding the Na ion plays a key role in ion pair dissociation. In contrast, Fig. 11(b) shows that, starting from the associated state ( $p_B \approx 0$ ),  $G_{1217}^5$  initially increases together with  $r_{\text{ion}}$  as the system approaches the TS ( $p_B = 0.5$ ). Upon crossing the separatrix line, however,  $G_{1217}^5$  decreases as the system proceeds toward the dissociated state ( $p_B \approx 1$ ). This behavior implies that dissociation is associated with a reduction in the population of water O atoms simultaneously belonging to the Na and Cl hydration shells. Thus, the two ACSFs,  $G_{58}^5$  and  $G_{1217}^5$ , identified through the SHAP analysis highlight the central role of solvent environments in the association and dissociation of NaCl ion pairs in water.

Finally, we conducted a comparative analysis of the correlation between  $G_{58}^5$  and  $G_{1217}^5$  and  $\rho$  and  $N_B$ , identified as CVs representing water bridging structures (see definitions of  $\rho$  and  $N_B$  in Section IID).<sup>65</sup> Figure 12 shows the distribution of the committor  $p_B^*$  on two-dimensional planes defined by the variable combinations  $(G_{58}^5, \rho)$  (a),  $(G_{1217}^5, \rho)$  (b),  $(G_{58}^5, N_B)$  (c), and  $(G_{1217}^5, N_B)$  (d). The correlation coefficient,  $r$ , for each variable pair is also reported in Fig. 12. The interionic water density  $\rho$  exhibits a positive correlation with  $G_{58}^5$  and a weak negative correlation with  $G_{1217}^5$ . Similarly, the number of bridging water molecules  $N_B$  shows a positive correlation with  $G_{58}^5$ , while its correlation with  $G_{1217}^5$  is slightly stronger than that observed for  $\rho$ . Thus, increases in  $\rho$  and  $N_B$ , which correlate positively with  $G_{58}^5$  and negatively with  $G_{1217}^5$ , are associated with dissociation from the associated state, consistent with the separatrix line observed in Fig. 11. Moreover, the committor distributions in each panel of Fig. 11 display a clear separation between associated and dissociated states. Overall, the two CVs,  $\rho$  and  $N_B$ , are confirmed as key contributors to the RC through their correspondence with the two ACSF descriptors  $G_{58}^5$  and  $G_{1217}^5$ .

#### IV. SUMMARY AND OUTLOOK

In this review, we have presented an explainable deep learning framework for identifying RCs in complex molecular systems based on committor  $p_B^*$  sampling. By combining DNNs with model-agnostic interpretation techniques such as LIME and SHAP, this framework enables the identification of CVs that contribute significantly to the RC while maintaining interpretability. Applications to representative systems, including the isomerization of alanine dipeptide and the association and dissociation of NaCl ion pairs in water, demonstrate that the framework can successfully extract physically meaningful

features governing their transition processes.

Furthermore, DNN models with diverse architectures, differing in the number of nodes, layers, and regularization parameters, describe the RC with comparable accuracy. The CVs identified through LIME and SHAP are highly consistent across different models, indicating that the hyperparameter space of the neural network is multimodal. This suggests that, although multiple model structures may achieve similar predictive performance, the underlying physical features that govern the transition mechanism remain robust.

These results highlight the potential of the explainable deep learning framework to systematically identify relevant CVs from high-dimensional configurational spaces. Compared with conventional approaches for describing PMFs, which often rely heavily on physical intuition and trial and error, the present framework provides a more data-driven strategy for constructing PMFs and interpreting the mechanism of transition pathways. Nevertheless, the reliability of the identified RCs depends on the selection of candidate CVs and the performance of the neural network model, emphasizing the importance of careful feature design and appropriate hyperparameter optimization.

Future developments are expected to further enhance the applicability of this framework to increasingly complex systems. In particular, improvements in the definition of CVs, integration with advanced sampling techniques, and the incorporation of more advanced machine learning architectures, such as graph neural networks,<sup>105,114,118,119</sup> will enable the analysis of larger and more complex molecular environments. In addition, the development of methods that combine interpretability with automated feature generation may reduce the dependence on predefined CVs. These advances will contribute to a deeper understanding of rare-event mechanisms in complex molecular systems and will expand the role of explainable deep learning in theoretical and computational chemistry.

#### ACKNOWLEDGMENTS

The authors acknowledge Yusuke Mori, Takuma Kikutsuji, Kazushi Okada, Kyohei Kawashima, Takumi Sato, and Kenji Okada for fruitful collaborations. This work was supported by JSPS KAKENHI Grant-in-Aid Grant Nos. JP23K23858, JP25H02299, JP23K23303, JP23KK0254, JP24K21756, JP25H02464, JP25K02235, JP25K00968, JP24H01719, JP22K03550, and JP23H02622. We acknowledge support from the Fugaku Supercomputing Project (Nos. JPMXP1020230325 and JPMXP1020230327) and the Data-Driven Material Research Project (No. JPMXP1122714694) from the Ministry of Education, Culture, Sports, Science, and Technology and by Maruho Collaborative Project for Theoretical Pharmaceuticals. The numerical calculations were performed at Research Center of Computational Science, Okazaki Research Facilities, National Institutes of Natural Sciences (Projects: 25-IMS-C052, 25-IMS-C105, 25-IMS-C227).

## AUTHOR DECLARATIONS

### Conflict of Interest

The authors have no conflicts to disclose.

### Data availability statement

No new data were generated or analyzed in this study; therefore, data sharing is not applicable.

- <sup>1</sup>D. M. Zuckerman, *Statistical Physics of Biomolecules: An Introduction* (CRC Press, Boca Raton, 2010).
- <sup>2</sup>G. Torrie and J. Valleau, "Nonphysical sampling distributions in Monte Carlo free-energy estimation: Umbrella sampling," *J. Comput. Phys.* **23**, 187–199 (1977).
- <sup>3</sup>Y. Sugita and Y. Okamoto, "Replica-exchange molecular dynamics method for protein folding," *Chem. Phys. Lett.* **314**, 141–151 (1999).
- <sup>4</sup>A. Laio and M. Parrinello, "Escaping free-energy minima," *Proc. Natl. Acad. Sci. U.S.A.* **99**, 12562–12566 (2002).
- <sup>5</sup>C. Chipot, A. Pohorille, A. W. Castleman, J. P. Toennies, K. Yamanouchi, and W. Zinth, eds., *Free Energy Calculations: Theory and Applications in Chemistry and Biology* (Springer, Berlin, 2007).
- <sup>6</sup>M. E. Tuckerman, *Statistical Mechanics: Theory and Molecular Simulation*, 2nd ed. (Oxford University Press, Oxford, 2023).
- <sup>7</sup>D. Frenkel and B. Smit, *Understanding Molecular Simulation: From Algorithms to Applications* (Academic Press, Amsterdam, 2023).
- <sup>8</sup>C. Chipot, "Free Energy Methods for the Description of Molecular Processes," *Annu. Rev. Biophys.* **52**, 113–138 (2023).
- <sup>9</sup>B. Peters, *Reaction Rate Theory and Rare Events* (Elsevier, Amsterdam, 2017).
- <sup>10</sup>D. Frenkel, "Simulations: The dark side," *Eur. Phys. J. Plus* **128**, 10 (2013).
- <sup>11</sup>T. Nakamura, "Derivation of the Invariant Free-Energy Landscape Based on Langevin Dynamics," *Phys. Rev. Lett.* **132**, 137101 (2024).
- <sup>12</sup>P. G. Bolhuis, D. Chandler, C. Dellago, and P. L. Geissler, "Transition Path Sampling: Throwing Ropes Over Rough Mountain Passes, in the Dark," *Annu. Rev. Phys. Chem.* **53**, 291–318 (2002).
- <sup>13</sup>M. A. Rohrdanz, W. Zheng, and C. Clementi, "Discovering Mountain Passes via Torchlight: Methods for the Definition of Reaction Coordinates and Pathways in Complex Macromolecular Reactions," *Annu. Rev. Phys. Chem.* **64**, 295–316 (2013).
- <sup>14</sup>S. Jungblut and C. Dellago, "Pathways to self-organization: Crystallization via nucleation and growth," *Eur. Phys. J. E* **39**, 77 (2016).
- <sup>15</sup>P. V. Banushkina and S. V. Krivov, "Optimal reaction coordinates," *WIREs Comput. Mol. Sci.* **6**, 748–763 (2016).
- <sup>16</sup>J. Rogal, "Reaction coordinates in complex systems—a perspective," *Eur. Phys. J. B* **94**, 223 (2021).
- <sup>17</sup>F. Pietrucci, "Strategies for the exploration of free energy landscapes: Unity in diversity and challenges ahead," *Rev. Phys.* **2**, 32–45 (2017).
- <sup>18</sup>R. Du, V. S. Pande, A. Y. Grosberg, T. Tanaka, and E. S. Shakhnovich, "On the transition coordinate for protein folding," *J. Chem. Phys.* **108**, 334–350 (1998).
- <sup>19</sup>P. L. Geissler, C. Dellago, and D. Chandler, "Kinetic Pathways of Ion Pair Dissociation in Water," *J. Phys. Chem. B* **103**, 3706–3710 (1999).
- <sup>20</sup>P. G. Bolhuis, C. Dellago, and D. Chandler, "Reaction coordinates of biomolecular isomerization," *Proc. Natl. Acad. Sci. U.S.A.* **97**, 5877–5882 (2000).
- <sup>21</sup>M. F. Hagan, A. R. Dinner, D. Chandler, and A. K. Chakraborty, "Atomistic understanding of kinetic pathways for single base-pair binding and unbinding in DNA," *Proc. Natl. Acad. Sci. U.S.A.* **100**, 13922–13927 (2003).
- <sup>22</sup>G. Hummer, "From transition paths to transition states and rate coefficients," *J. Chem. Phys.* **120**, 516–523 (2004).
- <sup>23</sup>A. C. Pan and D. Chandler, "Dynamics of Nucleation in the Ising Model," *J. Phys. Chem. B* **108**, 19681–19686 (2004).
- <sup>24</sup>W. Ren, E. Vanden-Eijnden, P. Maragakis, and W. E., "Transition pathways in complex systems: Application of the finite-temperature string method to the alanine dipeptide," *J. Chem. Phys.* **123**, 134109 (2005).
- <sup>25</sup>Y. M. Rhee and V. S. Pande, "One-Dimensional Reaction Coordinate and the Corresponding Potential of Mean Force from Commitment Probability Distribution," *J. Phys. Chem. B* **109**, 6780–6786 (2005).
- <sup>26</sup>W. E, W. Ren, and E. Vanden-Eijnden, "Transition pathways in complex systems: Reaction coordinates, isocommittor surfaces, and transition tubes," *Chem. Phys. Lett.* **413**, 242–247 (2005).
- <sup>27</sup>A. Berezhkovskii and A. Szabo, "One-dimensional reaction coordinates for diffusive activated rate processes in many dimensions," *J. Chem. Phys.* **122**, 014503 (2005).
- <sup>28</sup>R. B. Best and G. Hummer, "Reaction coordinates and rates from transition paths," *Proc. Natl. Acad. Sci. U.S.A.* **102**, 6732–6737 (2005).
- <sup>29</sup>D. Moroni, P. R. ten Wolde, and P. G. Bolhuis, "Interplay between Structure and Size in a Critical Crystal Nucleus," *Phys. Rev. Lett.* **94**, 235703 (2005).
- <sup>30</sup>L. Maragliano, A. Fischer, E. Vanden-Eijnden, and G. Ciccotti, "String method in collective variables: Minimum free energy paths and isocommittor surfaces," *J. Chem. Phys.* **125**, 024106 (2006).
- <sup>31</sup>B. Peters, "Using the histogram test to quantify reaction coordinate error," *J. Chem. Phys.* **125**, 241101 (2006).
- <sup>32</sup>D. Branduardi, F. L. Gervasio, and M. Parrinello, "From A to B in free energy space," *J. Chem. Phys.* **126**, 054103 (2007).
- <sup>33</sup>S. L. Quaytman and S. D. Schwartz, "Reaction coordinate of an enzymatic reaction revealed by transition path sampling," *Proc. Natl. Acad. Sci. U.S.A.* **104**, 12253–12258 (2007).
- <sup>34</sup>D. Antoniou and S. D. Schwartz, "Toward Identification of the Reaction Coordinate Directly from the Transition State Ensemble Using the Kernel PCA Method," *J. Phys. Chem. B* **115**, 2465–2469 (2011).
- <sup>35</sup>A. J. Ballard and C. Dellago, "Toward the Mechanism of Ionic Dissociation in Water," *J. Phys. Chem. B* **116**, 13490–13497 (2012).
- <sup>36</sup>B. C. Barnes, B. C. Knott, G. T. Beckham, D. T. Wu, and A. K. Sum, "Reaction Coordinate of Incipient Methane Clathrate Hydrate Nucleation," *J. Phys. Chem. B* **118**, 13236–13243 (2014).
- <sup>37</sup>E. Pluhařová, M. D. Baer, G. K. Schenter, P. Jungwirth, and C. J. Mundy, "Dependence of the Rate of LiF Ion-Pairing on the Description of Molecular Interaction," *J. Phys. Chem. B* **120**, 1749–1758 (2016).
- <sup>38</sup>Q. Li, B. Lin, and W. Ren, "Computing committor functions for the study of rare events using deep learning," *J. Chem. Phys.* **151**, 054112 (2019).
- <sup>39</sup>Z. F. Brotzakis and P. G. Bolhuis, "Approximating free energy and committor landscapes in standard transition path sampling using virtual interface exchange," *J. Chem. Phys.* **151**, 174111 (2019).
- <sup>40</sup>F. Manuchehrfar, H. Li, W. Tian, A. Ma, and J. Liang, "Exact Topology of the Dynamic Probability Surface of an Activated Process by Persistent Homology," *J. Phys. Chem. B* **125**, 4667–4680 (2021).
- <sup>41</sup>S. Wu, H. Li, and A. Ma, "A Rigorous Method for Identifying a One-Dimensional Reaction Coordinate in Complex Molecules," *J. Chem. Theory Comput.* **18**, 2836–2844 (2022).
- <sup>42</sup>S. Wu, H. Li, and A. Ma, "Exact reaction coordinates for flap opening in HIV-1 protease," *Proc. Natl. Acad. Sci. U.S.A.* **119**, e2214906119 (2022).
- <sup>43</sup>M. R. Hasyim, C. H. Batton, and K. K. Mandadapu, "Supervised learning and the finite-temperature string method for computing committor functions and reaction rates," *J. Chem. Phys.* **157**, 184111 (2022).
- <sup>44</sup>K. Mochizuki, K.-i. Murata, and X. Zhang, "Microscopic ordering of supercooled water on the ice basal face," *Commun. Mater.* **4**, 1–10 (2023).
- <sup>45</sup>H. Li and A. Ma, "Enhanced sampling of protein conformational changes via true reaction coordinates from energy relaxation," *Nat. Commun.* **16**, 786 (2025).
- <sup>46</sup>D. T. Zhang, L. Baldauf, G. Lazarski, T. S. Van Erp, and W. Shinoda, "Membrane Pore Formation Unveiled by  $\infty$ RETIS Path Sampling: From Thinning to Flip-Flop," *J. Chem. Theory Comput.* **22**, 3072–3083 (2026).
- <sup>47</sup>B. Peters, "Recent advances in transition path sampling: Accurate reaction coordinates, likelihood maximisation and diffusive barrier-crossing dynamics," *Mol. Simul.* **36**, 1265–1281 (2010).
- <sup>48</sup>W. Li and A. Ma, "Recent Developments in Methods for Identifying Reaction Coordinates," *Mol. Simul.* **40**, 784–793 (2014).
- <sup>49</sup>B. Peters, "Reaction Coordinates and Mechanistic Hypothesis Tests," *Annu. Rev. Phys. Chem.* **67**, 669–690 (2016).
- <sup>50</sup>F. Sittel and G. Stock, "Perspective: Identification of collective variables

- and metastable states of protein dynamics,” *J. Chem. Phys.* **149**, 150901 (2018).
- <sup>51</sup>A. Ma and A. R. Dinner, “Automatic Method for Identifying Reaction Coordinates in Complex Systems,” *J. Phys. Chem. B* **109**, 6769–6779 (2005).
- <sup>52</sup>B. Peters and B. L. Trout, “Obtaining reaction coordinates by likelihood maximization,” *J. Chem. Phys.* **125**, 054108 (2006).
- <sup>53</sup>B. Peters, G. T. Beckham, and B. L. Trout, “Extensions to the likelihood maximization approach for finding reaction coordinates,” *J. Chem. Phys.* **127**, 034109 (2007).
- <sup>54</sup>G. T. Beckham, B. Peters, C. Starbuck, N. Variankaval, and B. L. Trout, “Surface-Mediated Nucleation in the Solid-State Polymorph Transformation of Terephthalic Acid,” *J. Am. Chem. Soc.* **129**, 4714–4723 (2007).
- <sup>55</sup>G. T. Beckham, B. Peters, and B. L. Trout, “Evidence for a Size Dependent Nucleation Mechanism in Solid State Polymorph Transformations,” *J. Phys. Chem. B* **112**, 7460–7466 (2008).
- <sup>56</sup>B. Peters, “Transition-State Theory, Dynamics, and Narrow Time Scale Separation in the Rate-Promoting Vibrations Model of Enzyme Catalysis,” *J. Chem. Theory Comput.* **6**, 1447–1454 (2010).
- <sup>57</sup>J. Vreede, J. Juraszek, and P. G. Bolhuis, “Predicting the reaction coordinates of millisecond light-induced conformational changes in photoactive yellow protein,” *Proc. Natl. Acad. Sci. U.S.A.* **107**, 2397–2402 (2010).
- <sup>58</sup>W. Lechner, J. Rogal, J. Juraszek, B. Ensing, and P. G. Bolhuis, “Nonlinear reaction coordinate analysis in the reweighted path ensemble,” *J. Chem. Phys.* **133**, 174110 (2010).
- <sup>59</sup>B. Pan and M. S. Ricci, “Molecular Mechanism of Acid-Catalyzed Hydrolysis of Peptide Bonds Using a Model Compound,” *J. Phys. Chem. B* **114**, 4389–4399 (2010).
- <sup>60</sup>G. T. Beckham and B. Peters, “Optimizing Nucleus Size Metrics for Liquid–Solid Nucleation from Transition Paths of Near-Nanosecond Duration,” *J. Phys. Chem. Lett.* **2**, 1133–1138 (2011).
- <sup>61</sup>B. Peters, “Inertial likelihood maximization for reaction coordinates with high transmission coefficients,” *Chem. Phys. Lett.* **554**, 248–253 (2012).
- <sup>62</sup>J. Juraszek, J. Vreede, and P. G. Bolhuis, “Transition path sampling of protein conformational changes,” *Chem. Phys.* **396**, 30–44 (2012).
- <sup>63</sup>L. Xi, M. Shah, and B. L. Trout, “Hopping of Water in a Glassy Polymer Studied via Transition Path Sampling and Likelihood Maximization,” *J. Phys. Chem. B* **117**, 3634–3647 (2013).
- <sup>64</sup>S. Jungblut, A. Singraber, and C. Dellago, “Optimising reaction coordinates for crystallisation by tuning the crystallinity definition,” *Mol. Phys.* **111**, 3527–3533 (2013).
- <sup>65</sup>R. G. Mullen, J.-E. Shea, and B. Peters, “Transmission Coefficients, Committors, and Solvent Coordinates in Ion-Pair Dissociation,” *J. Chem. Theory Comput.* **10**, 659–667 (2014).
- <sup>66</sup>R. G. Mullen, J.-E. Shea, and B. Peters, “Easy Transition Path Sampling Methods: Flexible-Length Aimless Shooting and Permutation Shooting,” *J. Chem. Theory Comput.* **11**, 2421–2428 (2015).
- <sup>67</sup>L. Lupi, B. Peters, and V. Molinero, “Pre-ordering of interfacial water in the pathway of heterogeneous ice nucleation does not lead to a two-step crystallization mechanism,” *J. Chem. Phys.* **145**, 211910 (2016).
- <sup>68</sup>L. Lupi, A. Hudait, B. Peters, M. Grünwald, R. Gotchy Mullen, A. H. Nguyen, and V. Molinero, “Role of stacking disorder in ice nucleation,” *Nature* **551**, 218–222 (2017).
- <sup>69</sup>H. Jung, K.-i. Okazaki, and G. Hummer, “Transition path sampling of rare events by shooting from the top,” *J. Chem. Phys.* **147**, 152716 (2017).
- <sup>70</sup>M. N. Joswiak, M. F. Doherty, and B. Peters, “Ion dissolution mechanism and kinetics at kink sites on NaCl surfaces,” *Proc. Natl. Acad. Sci. U.S.A.* **115**, 656–661 (2018).
- <sup>71</sup>G. Díaz Leines and J. Rogal, “Maximum Likelihood Analysis of Reaction Coordinates during Solidification in Ni,” *J. Phys. Chem. B* **122**, 10934–10942 (2018).
- <sup>72</sup>K.-i. Okazaki, D. Wöhlert, J. Warnau, H. Jung, Ö. Yildiz, W. Kühlbrandt, and G. Hummer, “Mechanism of the electroneutral sodium/proton antiporter PaNhaP from transition-path shooting,” *Nat. Commun.* **10**, 1742 (2019).
- <sup>73</sup>Arjun, T. A. Berendsen, and P. G. Bolhuis, “Unbiased atomistic insight in the competing nucleation mechanisms of methane hydrates,” *Proc. Natl. Acad. Sci. USA* **116**, 19305–19310 (2019).
- <sup>74</sup>M. Marriott, L. Lupi, A. Kumar, and V. Molinero, “Following the nucleation pathway from disordered liquid to gyroid mesophase,” *J. Chem. Phys.* **150**, 164902 (2019).
- <sup>75</sup>Y. Liang, G. Díaz Leines, R. Drautz, and J. Rogal, “Identification of a multi-dimensional reaction coordinate for crystal nucleation in Ni<sub>3</sub>Al,” *J. Chem. Phys.* **152**, 224504 (2020).
- <sup>76</sup>J. R. Rogers and P. L. Geissler, “Breakage of Hydrophobic Contacts Limits the Rate of Passive Lipid Exchange between Membranes,” *J. Phys. Chem. B* **124**, 5884–5898 (2020).
- <sup>77</sup>N. Schwierz, “Kinetic pathways of water exchange in the first hydration shell of magnesium,” *J. Chem. Phys.* **152**, 224106 (2020).
- <sup>78</sup>L. Levintov, S. Paul, and H. Vashisth, “Reaction Coordinate and Thermodynamics of Base Flipping in RNA,” *J. Chem. Theory Comput.* **17**, 1914–1921 (2021).
- <sup>79</sup>R. L. Silveira, B. C. Knott, C. S. Pereira, M. F. Crowley, M. S. Skaf, and G. T. Beckham, “Transition Path Sampling Study of the Feruloyl Esterase Mechanism,” *J. Phys. Chem. B* **125**, 2018–2030 (2021).
- <sup>80</sup>W. Li, “Optimizing reaction coordinate by flux maximization in the transition path ensemble,” *J. Chem. Phys.* **156**, 054117 (2022).
- <sup>81</sup>E. Schneider, L. Dai, R. Q. Topper, C. Drechsel-Grau, and M. E. Tuckerman, “Stochastic Neural Network Approach for Learning High-Dimensional Free Energy Surfaces,” *Phys. Rev. Lett.* **119**, 150601 (2017).
- <sup>82</sup>R. T. McGibbon, B. E. Husic, and V. S. Pande, “Identification of simple reaction coordinates from complex dynamics,” *J. Chem. Phys.* **146**, 044109 (2017).
- <sup>83</sup>M. M. Sultan and V. S. Pande, “Automated design of collective variables using supervised machine learning,” *J. Chem. Phys.* **149**, 094106 (2018).
- <sup>84</sup>C. Wehmeyer and F. Noé, “Time-lagged autoencoders: Deep learning of slow collective variables for molecular kinetics,” *J. Chem. Phys.* **148**, 241703 (2018).
- <sup>85</sup>W. Chen and A. L. Ferguson, “Molecular enhanced sampling with autoencoders: On-the-fly collective variable discovery and accelerated free energy landscape exploration,” *J. Comput. Chem.* **39**, 2079–2102 (2018).
- <sup>86</sup>J. M. L. Ribeiro, P. Bravo, Y. Wang, and P. Tiwary, “Reweighted autoencoded variational Bayes for enhanced sampling (RAVE),” *J. Chem. Phys.* **149**, 072301 (2018).
- <sup>87</sup>A. Mardt, L. Pasquali, H. Wu, and F. Noé, “VAMPnets for deep learning of molecular kinetics,” *Nat. Commun.* **9**, 5 (2018).
- <sup>88</sup>A. Bittracher, R. Banisch, and C. Schütte, “Data-driven computation of molecular reaction coordinates,” *J. Chem. Phys.* **149**, 154103 (2018).
- <sup>89</sup>J. Rogal, E. Schneider, and M. E. Tuckerman, “Neural-Network-Based Path Collective Variables for Enhanced Sampling of Phase Transformations,” *Phys. Rev. Lett.* **123**, 245701 (2019).
- <sup>90</sup>L. Bonati, V. Rizzi, and M. Parrinello, “Data-Driven Collective Variables for Enhanced Sampling,” *J. Phys. Chem. Lett.* **11**, 2998–3004 (2020).
- <sup>91</sup>L. Bonati, G. Piccini, and M. Parrinello, “Deep learning the slow modes for rare events sampling,” *Proc. Natl. Acad. Sci. U.S.A.* **118**, e2113533118 (2021).
- <sup>92</sup>D. Wang and P. Tiwary, “State predictive information bottleneck,” *J. Chem. Phys.* **154**, 134111 (2021).
- <sup>93</sup>J. Zhang, Y.-K. Lei, Z. Zhang, X. Han, M. Li, L. Yang, Y. I. Yang, and Y. Q. Gao, “Deep reinforcement learning of transition states,” *Phys. Chem. Chem. Phys.* **23**, 6888–6895 (2021).
- <sup>94</sup>F. Hooft, A. Pérez de Alba Ortíz, and B. Ensing, “Discovering Collective Variables of Molecular Transitions via Genetic Algorithms and Neural Networks,” *J. Chem. Theory Comput.* **17**, 2294–2306 (2021).
- <sup>95</sup>T. Magrino, L. Huet, A. M. Saitta, and F. Pietrucci, “Critical Assessment of Data-Driven versus Heuristic Reaction Coordinates in Solution Chemistry,” *J. Phys. Chem. A* **126**, 8887–8900 (2022).
- <sup>96</sup>Z. Belkacemi, P. Gkeka, T. Lelièvre, and G. Stoltz, “Chasing Collective Variables Using Autoencoders and Biased Trajectories,” *J. Chem. Theory Comput.* **18**, 59–78 (2022).
- <sup>97</sup>J. Baima, A. M. Goryaeva, T. D. Swinburne, J.-B. Maillat, M. Nastar, and M.-C. Marinica, “Capabilities and limits of autoencoders for extracting collective variables in atomistic materials science,” *Phys. Chem. Chem. Phys.* **24**, 23152–23163 (2022).
- <sup>98</sup>L. Sun, J. Vandermause, S. Batzner, Y. Xie, D. Clark, W. Chen, and B. Kozinsky, “Multitask Machine Learning of Collective Variables for Enhanced Sampling of Rare Events,” *J. Chem. Theory Comput.* **18**, 2341–2353 (2022).
- <sup>99</sup>R. Ketkaew and S. Luber, “DeepCV: A Deep Learning Framework for Blind Search of Collective Variables in Expanded Configurational Space,” *J. Chem. Inf. Model.* , acs.jcim.2c00883 (2022).

- <sup>100</sup>G. Lazzari, H. Jung, P. G. Bolhuis, and R. Covino, "Molecular Free Energies, Rates, and Mechanisms from Data-Efficient Path Sampling Simulations," *J. Chem. Theory Comput.* **19**, 9060–9076 (2023).
- <sup>101</sup>H. Chen, B. Roux, and C. Chipot, "Discovering Reaction Pathways, Slow Variables, and Committor Probabilities with Machine Learning," *J. Chem. Theory Comput.* **19**, 4414–4426 (2023).
- <sup>102</sup>A. N. Singh and D. T. Limmer, "Variational deep learning of equilibrium transition path ensembles," *J. Chem. Phys.* **159**, 024124 (2023).
- <sup>103</sup>S. Liang, A. N. Singh, Y. Zhu, D. T. Limmer, and C. Yang, "Probing reaction channels via reinforcement learning," *Mach. Learn.: Sci. Technol.* **4**, 045003 (2023).
- <sup>104</sup>A. France-Lanord, H. Vroylandt, M. Salanne, B. Rotenberg, A. M. Saitta, and F. Pietrucci, "Data-Driven Path Collective Variables," *J. Chem. Theory Comput.* **20**, 3069–3084 (2024).
- <sup>105</sup>J. Zhang, L. Bonati, E. Trizio, O. Zhang, Y. Kang, T. Hou, and M. Parrinello, "Descriptor-Free Collective Variables from Geometric Graph Neural Networks," *J. Chem. Theory Comput.* **20**, 10787–10797 (2024).
- <sup>106</sup>J. Zhang, O. Zhang, L. Bonati, and T. Hou, "Combining Transition Path Sampling with Data-Driven Collective Variables through a Reactivity-Biased Shooting Algorithm," *J. Chem. Theory Comput.* **20**, 4523–4532 (2024).
- <sup>107</sup>N. S. M. Herringer, S. Dasetty, D. Gandhi, J. Lee, and A. L. Ferguson, "Permutationally Invariant Networks for Enhanced Sampling (PINES): Discovery of Multimolecular and Solvent-Inclusive Collective Variables," *J. Chem. Theory Comput.* **20**, 178–198 (2024).
- <sup>108</sup>T. Fröhling, L. Bonati, V. Rizzi, and F. L. Gervasio, "Deep learning path-like collective variable for enhanced sampling molecular dynamics," *J. Chem. Phys.* **160**, 174109 (2024).
- <sup>109</sup>P. Kang, E. Trizio, and M. Parrinello, "Computing the committor with the committor to study the transition state ensemble," *Nat. Comput. Sci.* , 1–10 (2024).
- <sup>110</sup>A. Megías, S. Contreras Arredondo, C. G. Chen, C. Tang, B. Roux, and C. Chipot, "Iterative variational learning of committor-consistent transition pathways using artificial neural networks," *Nat. Comput. Sci.* **5**, 592–602 (2025).
- <sup>111</sup>B. Liu, S. Cao, J. G. Boysen, M. Xue, and X. Huang, "Memory kernel minimization-based neural networks for discovering slow collective variables of biomolecular dynamics," *Nat. Comput. Sci.* **5**, 562–571 (2025).
- <sup>112</sup>R. Elangovan, S. Chatterjee, and D. Ray, "Data-driven enhanced sampling of mechanistic pathways," *Proc. Natl. Acad. Sci. U.S.A.* **122**, e2517169122 (2025).
- <sup>113</sup>F. M. Dietrich and M. Salvalaglio, "On the reproducibility of free energy surfaces in machine-learned collective variable spaces," *J. Chem. Phys.* **163**, 141102 (2025).
- <sup>114</sup>Z. Pengmei, C. Lorpaiboon, S. C. Guo, J. Weare, and A. R. Dinner, "Using pretrained graph neural networks with token mixers as geometric featurizers for conformational dynamics," *J. Chem. Phys.* **162**, 044107 (2025).
- <sup>115</sup>P. R. Prabhakar, D. Ray, and I. Andricioaei, "Discriminant analysis optimizes progress coordinate in weighted ensemble simulations of rare event kinetics," *J. Chem. Phys.* **163**, 074111 (2025).
- <sup>116</sup>J. J. Kresse, A. Sikorski, V. Sunkara, S. Chewle, and M. Weber, "Revealing the Atomistic Mechanism of Rare Events in Molecular Dynamics," *J. Chem. Theory Comput.* , acs.jctc.5c01906 (2026).
- <sup>117</sup>C. Giuseppe Chen, C. Tang, A. Megías, R. A. Talmazan, S. Contreras Arredondo, B. Roux, and C. Chipot, "Following the Committor Flow: A Data-Driven Discovery of Transition Pathways," *J. Chem. Theory Comput.* , acs.jctc.6c00007 (2026).
- <sup>118</sup>S. Contreras Arredondo, C. Tang, R. A. Talmazan, A. Megías, C. G. Chen, and C. Chipot, "Learning the committor without collective variables," *Nat. Comput. Sci.* (2026), 10.1038/s43588-026-00958-2.
- <sup>119</sup>P. Kang, J. Zhang, E. Trizio, T. Hou, and M. Parrinello, "Committors without Descriptors," *J. Chem. Theory Comput.* **22**, 1613–1620 (2026).
- <sup>120</sup>Y. Wang, J. M. Lamim Ribeiro, and P. Tiwary, "Machine learning approaches for analyzing and enhancing molecular dynamics simulations," *Curr. Opin. Struct. Biol.* **61**, 139–145 (2020).
- <sup>121</sup>H. Sidky, W. Chen, and A. L. Ferguson, "Machine learning for collective variable discovery and enhanced sampling in biomolecular simulation," *Mol. Phys.* **118**, e1737742 (2020).
- <sup>122</sup>F. Noé, A. Tkatchenko, K.-R. Müller, and C. Clementi, "Machine Learning for Molecular Simulation," *Annu. Rev. Phys. Chem.* **71**, 361–390 (2020).
- <sup>123</sup>M. Chen, "Collective variable-based enhanced sampling and machine learning," *Eur. Phys. J. B* **94**, 211 (2021).
- <sup>124</sup>H. Fu, H. Bian, X. Shao, and W. Cai, "Collective Variable-Based Enhanced Sampling: From Human Learning to Machine Learning," *J. Phys. Chem. Lett.* , 1774–1783 (2024).
- <sup>125</sup>S. Mehdi, Z. Smith, L. Herron, Z. Zou, and P. Tiwary, "Enhanced Sampling with Machine Learning," *Annu. Rev. Phys. Chem.* **75**, 347–370 (2024).
- <sup>126</sup>A. N. Singh, A. Das, and D. T. Limmer, "Variational Path Sampling of Rare Dynamical Events," *Annu. Rev. Phys. Chem.* **76**, 639–662 (2025).
- <sup>127</sup>T. Gökdemir and J. Rydzewski, "Machine learning of slow collective variables and enhanced sampling via spatial techniques," *Chem. Phys. Rev.* **6**, 011304 (2025).
- <sup>128</sup>K. Zhu, E. Trizio, J. Zhang, R. Hu, L. Jiang, T. Hou, and L. Bonati, "Enhanced Sampling in the Age of Machine Learning: Algorithms and Applications," *Chem. Rev.* , 671–713 (2026).
- <sup>129</sup>T. Kikutsuji, Y. Mori, K.-i. Okazaki, T. Mori, K. Kim, and N. Matubayasi, "Explaining reaction coordinates of alanine dipeptide isomerization obtained from deep neural networks using Explainable Artificial Intelligence (XAI)," *J. Chem. Phys.* **156**, 154108 (2022).
- <sup>130</sup>T. Mori and S. Saito, "Dissecting the Dynamics during Enzyme Catalysis: A Case Study of Pin1 Peptidyl-Prolyl Isomerase," *J. Chem. Theory Comput.* **16**, 3396–3407 (2020).
- <sup>131</sup>Y. Mori, K.-i. Okazaki, T. Mori, K. Kim, and N. Matubayasi, "Learning reaction coordinates via cross-entropy minimization: Application to alanine dipeptide," *J. Chem. Phys.* **153**, 054115 (2020).
- <sup>132</sup>K. Kawashima, T. Sato, K.-i. Okazaki, K. Kim, N. Matubayasi, and T. Mori, "Investigating the hyperparameter space of deep neural network models for reaction coordinates," *APL Mach. Learn.* **3**, 016113 (2025).
- <sup>133</sup>A. Adadi and M. Berrada, "Peeking Inside the Black-Box: A Survey on Explainable Artificial Intelligence (XAI)," *IEEE Access* **6**, 52138–52160 (2018).
- <sup>134</sup>C. Molnar, *Interpretable Machine Learning* (Lulu.com, Morrisville, North Carolina, 2020).
- <sup>135</sup>M. T. Ribeiro, S. Singh, and C. Guestrin, "'Why Should I Trust You?': Explaining the Predictions of Any Classifier," in *Proceedings of the 22nd ACM SIGKDD International Conference on Knowledge Discovery and Data Mining* (Association for Computing Machinery, San Francisco California, U.S.A., 2016) pp. 1135–1144.
- <sup>136</sup>S. M. Lundberg and S.-I. Lee, "A unified approach to interpreting model predictions," in *Proceedings of the 31st international conference on neural information processing systems* (Curran Associates Inc., Red Hook, NY, 2017) pp. 4768–4777.
- <sup>137</sup>K. Okada, T. Kikutsuji, K.-i. Okazaki, T. Mori, K. Kim, and N. Matubayasi, "Unveiling interatomic distances influencing the reaction coordinates in alanine dipeptide isomerization: An explainable deep learning approach," *J. Chem. Phys.* **160**, 174110 (2024).
- <sup>138</sup>J. Behler and M. Parrinello, "Generalized Neural-Network Representation of High-Dimensional Potential-Energy Surfaces," *Phys. Rev. Lett.* **98**, 146401 (2007).
- <sup>139</sup>J. Behler, "Atom-centered symmetry functions for constructing high-dimensional neural network potentials," *J. Chem. Phys.* **134**, 074106 (2011).
- <sup>140</sup>J. Behler, "Perspective: Machine learning potentials for atomistic simulations," *J. Chem. Phys.* **145**, 170901 (2016).
- <sup>141</sup>K. Okada, K. Okada, K.-i. Okazaki, T. Mori, K. Kim, and N. Matubayasi, "Deep learning of committor for ion dissociation and interpretable analysis of solvent effects using atom-centered symmetry functions," *J. Chem. Phys.* **164**, 094101 (2026).
- <sup>142</sup>M. Frassek, A. Arjun, and P. G. Bolhuis, "An extended autoencoder model for reaction coordinate discovery in rare event molecular dynamics datasets," *J. Chem. Phys.* **155**, 064103 (2021).
- <sup>143</sup>H. Jung, R. Covino, A. Arjun, C. Leitold, C. Dellago, P. G. Bolhuis, and G. Hummer, "Machine-guided path sampling to discover mechanisms of molecular self-organization," *Nat. Comput. Sci.* **3**, 334–345 (2023).
- <sup>144</sup>J. Neumann and N. Schwierz, "Artificial Intelligence Resolves Kinetic Pathways of Magnesium Binding to RNA," *J. Chem. Theory Comput.* **18**, 1202–1212 (2022).
- <sup>145</sup>G. Ke, Q. Meng, T. Finley, T. Wang, W. Chen, W. Ma, Q. Ye, and T.-Y. Liu, "LightGBM: A Highly Efficient Gradient Boosting Decision Tree," in *Advances in Neural Information Processing Systems*, Vol. 30, edited

- by I. Guyon, U. V. Luxburg, S. Bengio, H. Wallach, R. Fergus, S. Vishwanathan, and R. Garnett (Curran Associates, Inc., 2017).
- <sup>146</sup>N. Naleem, C. R. A. Abreu, K. Warmuz, M. Tong, S. Kirmizialtin, and M. E. Tuckerman, "An exploration of machine learning models for the determination of reaction coordinates associated with conformational transitions," *J. Chem. Phys.* **159**, 034102 (2023).
- <sup>147</sup>B. C. Barnes, B. C. Knott, G. T. Beckham, D. T. Wu, and A. K. Sum, "Reaction Coordinate of Incipient Methane Clathrate Hydrate Nucleation," *J. Phys. Chem. B* **118**, 13236–13243 (2014).
- <sup>148</sup>P. J. Steinhardt, D. R. Nelson, and M. Ronchetti, "Bond-orientational order in liquids and glasses," *Phys. Rev. B* **28**, 784–805 (1983).
- <sup>149</sup>W. Lechner and C. Dellago, "Accurate determination of crystal structures based on averaged local bond order parameters," *J. Chem. Phys.* **129**, 114707 (2008).
- <sup>150</sup>Y. Yonetani, "Distinct dissociation kinetics between ion pairs: Solvent-coordinate free-energy landscape analysis," *J. Chem. Phys.* **143**, 044506 (2015).
- <sup>151</sup>Y. Yonetani, "Solvent-coordinate free-energy landscape view of water-mediated ion-pair dissociation," *Mol. Phys.* **115**, 2987–2998 (2017).
- <sup>152</sup>M. Salanne, S. Tazi, R. Vuilleumier, and B. Rotenberg, "Ca<sup>2+</sup>-Cl<sup>-</sup> Association in Water Revisited: The Role of Cation Hydration," *ChemPhysChem* **18**, 2807–2811 (2017).
- <sup>153</sup>M. I. Oh, M. Gupta, and D. F. Weaver, "Understanding Water Structure in an Ion-Pair Solvation Shell in the Vicinity of a Water/Membrane Interface," *J. Phys. Chem. B* **123**, 3945–3954 (2019).
- <sup>154</sup>C. Zhang, F. Giberti, E. Sevgen, J. J. de Pablo, F. Gygi, and G. Galli, "Dissociation of salts in water under pressure," *Nat. Commun.* **11**, 3037 (2020).
- <sup>155</sup>D. Wang, R. Zhao, J. D. Weeks, and P. Tiwary, "Influence of Long-Range Forces on the Transition States and Dynamics of NaCl Ion-Pair Dissociation in Water," *J. Phys. Chem. B* **126**, 545–551 (2022).
- <sup>156</sup>K. Wilke, S. Tao, S. Calero, A. Lervik, and T. S. van Erp, "NaCl Dissociation Explored Through Predictive Power Path Sampling Analysis," *J. Chem. Theory Comput.* **21**, 4604–4614 (2025).
- <sup>157</sup>L. S. Shapley, "17. A Value for n-Person Games," in *Contributions to the Theory of Games (AM-28), Volume II*, edited by H. W. Kuhn and A. W. Tucker (Princeton University Press, 1953) pp. 307–318.
- <sup>158</sup>G. N. Ramachandran and V. Sasisekharan, "Conformation of Polypeptides and Proteins," in *Advances in Protein Chemistry*, Vol. 23, edited by C. B. Anfinsen, M. L. Anson, J. T. Edsall, and F. M. Richards (1968) pp. 283–437.
- <sup>159</sup>O. A. Karim and J. Andrew. McCammon, "Dynamics of a sodium chloride ion pair in water," *J. Am. Chem. Soc.* **108**, 1762–1766 (1986).
- <sup>160</sup>O. A. Karim and J. A. McCammon, "Rate constants for ion pair formation and dissociation in water," *Chem. Phys. Lett.* **132**, 219–224 (1986).
- <sup>161</sup>G. Ciccotti, M. Ferrario, J. T. Hynes, and R. Kapral, "Constrained molecular dynamics and the mean potential for an ion pair in a polar solvent," *Chem. Phys.* **129**, 241–251 (1989).
- <sup>162</sup>G. Ciccotti, M. Ferrario, J. T. Hynes, and R. Kapral, "Dynamics of ion pair interconversion in a polar solvent," *J. Chem. Phys.* **93**, 7137–7147 (1990).
- <sup>163</sup>E. Guardia, R. Rey, and J. A. Padró, "Potential of mean force by constrained molecular dynamics: A sodium chloride ion-pair in water," *Chem. Phys.* **155**, 187–195 (1991).
- <sup>164</sup>R. Rey and E. Guardia, "Dynamical aspects of the sodium(1+)-chloride ion pair association in water," *J. Phys. Chem.* **96**, 4712–4718 (1992).
- <sup>165</sup>D. E. Smith and L. X. Dang, "Computer simulations of NaCl association in polarizable water," *J. Chem. Phys.* **100**, 3757–3766 (1994).
- <sup>166</sup>F. N. Brünig, J. O. Daldrop, and R. R. Netz, "Pair-Reaction Dynamics in Water: Competition of Memory, Potential Shape, and Inertial Effects," *J. Phys. Chem. B* **126**, 10295–10304 (2022).